Journal of Materials Chemistry B

Materials for biology and medicine

rsc.li/materials-b

ROYAL SOCIETY OF CHEMISTRY
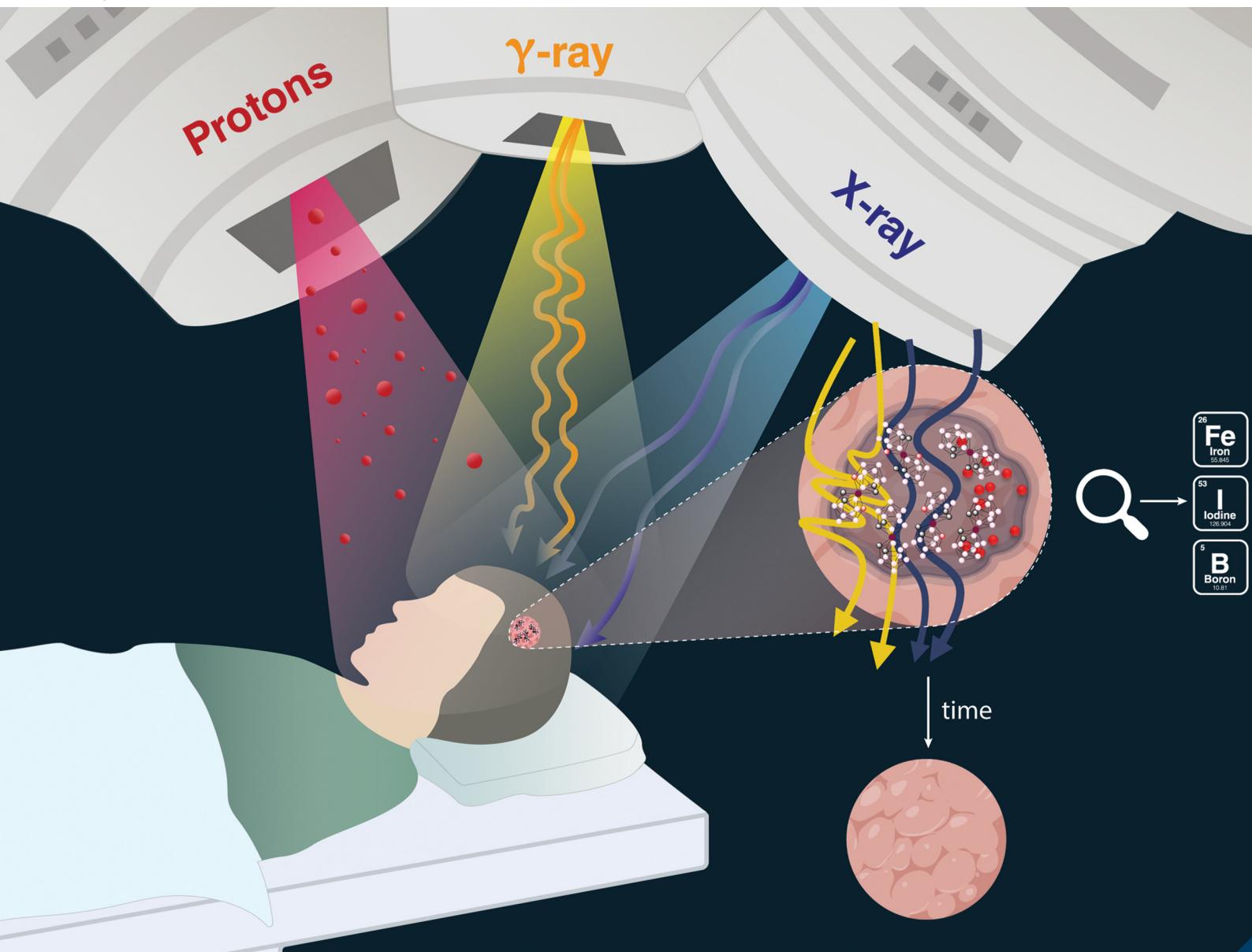
PAPER
Clara Viñas, Fernanda Marques *et al.*
Boron clusters (ferrabisdicarbollides) shaping the future as radiosensitizers for multimodal (chemo/radio/PBFR) therapy of glioblastoma

Indexed in Medline!

Check for updates

Boron clusters (ferrabisdicarbollides) shaping the future as radiosensitizers for multimodal (chemo/radio/PBFR) therapy of glioblastoma†

Miquel Nuez-Martínez,[a] María Queralt-Martín, [b] Amanda Muñoz-Juan,[a] Vicente M. Aguilella, [b] Anna Laromaine, [a] Francesc Teixidor, [a] Clara Viñas, [*a] Catarina G. Pinto,[c] Teresa Pinheiro, [d] Joana F. Guerreiro, [c] Filipa Mendes, [c] Catarina Roma-Rodrigues, [ef] Pedro V. Baptista, [ef] Alexandra R. Fernandes, [ef] Srecko Valic[g] and Fernanda Marques [*c]

Glioblastoma multiforme (GBM) is the most common and fatal primary brain tumor, and is highly resistant to conventional radiotherapy and chemotherapy. Therefore, the development of multidrug resistance and tumor recurrence are frequent. Given the poor survival with the current treatments, new therapeutic strategies are urgently needed. Radiotherapy (RT) is a common cancer treatment modality for GBM. However, there is still a need to improve RT efficiency, while reducing the severe side effects. Radiosensitizers can enhance the killing effect on tumor cells with less side effects on healthy tissues. Herein, we present our pioneering study on the highly stable and amphiphilic metallacarboranes, ferrabis(dicarbollides) ([o-FESAN]$^-$ and [8,8′-I2-o-FESAN]$^-$), as potential radiosensitizers for GBM radiotherapy. We propose radiation methodologies that utilize secondary radiation emissions from iodine and iron, using ferrabis(dicarbollides) as iodine/iron donors, aiming to achieve a greater therapeutic effect than that of a conventional radiotherapy. As a proof-of-concept, we show that using 2D and 3D models of U87 cells, the cellular viability and survival were reduced using this treatment approach. We also tested for the first time the proton boron fusion reaction (PBFR) with ferrabis(dicarbollides), taking advantage of their high boron (^{11}B) content. The results from the cellular damage response obtained suggest that proton boron fusion radiation therapy, when combined with boron-rich compounds, is a promising modality to fight against resistant tumors. Although these results are encouraging, more developments are needed to further explore ferrabis(dicarbollides) as radiosensitizers towards a positive impact on the therapeutic strategies for GBM.

[a] *Institut de Ciència de Materials de Barcelona, ICMAB-CSIC, Campus Universitat Autònoma de Barcelona, 08193 Bellaterra, Spain. E-mail: clara@icmab.es*

[b] *Laboratory of Molecular Biophysics, Department of Physics, Universitat Jaume I, 12071 Castelló, Spain*

[c] *Centro de Ciências e Tecnologias Nucleares e Departamento de Engenharia e Ciências Nucleares, Instituto Superior Técnico, Universidade de Lisboa, Estrada Nacional 10, 2695-066 Bobadela LRS, Portugal. E-mail: fmarujo@ctn.tecnico.ulisboa.pt*

[d] *iBB – Instituto de Bioengenharia e Biociências, Departamento de Engenharia e Ciências Nucleares, Instituto Superior Técnico, Universidade de Lisboa, Av. Rovisco Pais 1, 1049-001 Lisboa, Portugal*

[e] *UCIBIO – Applied Molecular Biosciences Unit, Department of Life Sciences, NOVA School of Science and Technology, NOVA University Lisbon, 2819-516 Caparica, Portugal*

[f] *Associate Laboratory i4HB – Institute for Health and Bioeconomy, NOVA School of Science and Technology, NOVA University Lisbon, 2819-516 Caparica, Portugal*

[g] *Ruđer Bošković Institute, Bijenička 54, HR-10000 Zagreb, Croatia*

† Electronic supplementary information (ESI) available: Scheme S1 and Fig. S1–S4. See DOI: https://doi.org/10.1039/d2tb01818g

1. Introduction

Cancer is a multifactorial disorder comprising a set of diseases arising from the uncontrolled growth and proliferation of abnormal cells because of the combined genetic and environmental factors. The core hallmarks of cancer include the abnormal cells' ability to sustain proliferative signaling, evade growth suppressors, induce angiogenesis, enable replicative immortality, resist cell death, and spread to other tissues and organs (metastasis).[1] Despite recent advances in therapeutics and diagnostics, cancer is still one of the leading causes of death worldwide, and given the ever-increasing number of new cases, clinical management of the disease continues to be a challenge in the 21st century.[2]

Currently, surgery, chemotherapy and radiotherapy are the most widely used cancer treatment modalities.[3,4] Their selection and application in therapeutic approaches depend on the

9794 | *J. Mater. Chem. B*, 2022, **10**, 9794–9815

This journal is © The Royal Society of Chemistry 2022

cancer type, location and stage of progression, in addition to the inherent complexity of tumor heterogeneity.[5]

Chemotherapy in cancer treatment is usually employed by administering cytostatic and/or cytotoxic drugs that halt tumor progression by suppressing the cells' ability to divide and induce apoptosis. However, most of the chemotherapeutic agents also target healthy cells, which results in severe dose-limiting side effects.[6] Moreover, patients exposed to prolonged chemotherapy regimens may acquire multidrug resistance (MDR) leading to treatment failure and relapse in most of the cases.[7]

Radiation therapy (RT) is an important cancer treatment modality, and approximately 50% of cancer patients receive radiation therapy during the course of their illness. The main goal of radiation therapy is to maximize the radiation dose to kill cancer cells, while sparing normal cells and tissues adjacent to or in the radiation path.[8] In the clinical setting, one of the most common approaches is to deliver high energy/high frequency electromagnetic radiation (X-rays and γ-rays) to tumor sites – external beam radiation. These electromagnetic X-rays and gamma rays are low-LET (Linear Energy Transfer) radiation sources composed of massless photons. Nevertheless, some of these therapeutic approaches still deliver radiation to normal tissues, thus increasing the risk of inducing additional cancers.[9]

Moreover, tumors resistant to radiation cannot be controlled even with high doses of radiation. Some new irradiation modalities are under development and include, for instance, particle beam therapy based on high-LET radiation[10] using particles with substantial mass and charge (alpha-particles, electrons, protons, and carbon ions), boron neutron capture therapy (BNCT)[11–14] using neutral particles such as neutrons and photodynamic therapy (PDT) – a light based technology that has also shown promising potential.[15] However, except PDT, these newer modalities can only typically be performed in larger medical facilities and, to date, have shown no evidence of clinical superiority compared to X-rays.[16,17] Although great success has been achieved with radiotherapy, further exploration of irradiation technologies is necessary to overcome the presented challenges.

A fundamental factor that needs to be considered in radiotherapy is the distribution of energy through the cells, which is of paramount importance when considering the biological damage done by a fixed dose of radiation. This distribution is influenced by the charge and mass of the particles that compose the radiation. One approach with the potential to enhance the success of radiation therapy is the use of radiosensitizers, whose purpose is to increase the radiation dose at tumor sites selectively, and, ultimately, to reduce the effective radiation dose and enhance the efficacy of treatment through a synergistic cell-killing effect when combined with radiation.[18,19] The main mechanisms include radiation-induced repair inhibition of DNA damage, increasing the degree of DNA damage, and disturbing the cell cycle and organelle function to improve cytotoxicity among others.

For a low radiation dose, the probability of the photoelectric effect and its concomitant Auger cascades or Compton scattering becomes significantly higher when a radiosensitizer is introduced within a targeted cell.[19]

Enriching tumors with high atomic number (Z) materials is an upcoming strategy to improve the effects of high-energy photons *via* amplifying of primary (electronic) processes.[20,21] As the photoelectric effect is dependent on the atomic number of the material, high Z materials have been used as radiosensitizers, taking advantage of their high attenuation capability for X-rays or gamma radiation. For instance, the use of gold (Au, Z = 79) nanomaterials as radiosensitizers has been greatly explored due to their ability to effectively absorb X-ray energy and interact with radiation in tumor cells, emitting photoelectrons, Auger electrons, and other secondary electrons and Compton scattering. These secondary electrons not only interact with DNA directly, but also react with water to increase the production of reactive oxygen species (ROS) and further increase the sensitivity of tumor cells to radiation.[22–25]

Iodine compounds were introduced as contrast agents for mammalian cell cultures; however, their application as radiosensitizers and therapeutic efficacy in radiotherapy have not been extensively studied. The use of iodine in radiation therapy has shown to enhance the cell killing effect of X-rays and cause chromosomal aberrations in irradiated cells.[26] Iodine possess four radioisotopes, $[^{123}I]^-$, $[^{124}I]^-$, $[^{125}I]^-$ and $[^{131}I]^-$,[27–31] that have been applied in medicine and biology in positron emission tomography (PET) or single photon emission computed tomography (SPECT) imaging and radiotherapy agents.[32,33] More recently, photon activation using iodine from iododeoxyuridine (IdUrd) and monochromatic photons above the K absorption edge of iodine (33.2 keV) as the activating agent exhibited a significant radiosensitization effect on glioblastoma. Nonetheless, due to their short circulation half-life and the inability to pass the blood brain barrier (BBB), iodinated compounds' clinical application has been limited.[34–36]

Metallacarboranes $[M(C_2B_9H_{11})_2]^-$ are unique 3D aromatics not only theoretically but also because of their advantages of high stability,[37] and water-soluble[38] and redox-active nature,[39] in which a central metal ion, commonly Co or Fe, is the common vertex of two joined by one vertex icosahedron.[40–44] These compounds share the versatility of the carboranes while the metal center introduces additional properties in redox potentials and the overall charge of the molecule. Characteristic properties of the small anionic metallabis(dicarbollide) molecules are their chemical and thermal stability (withstanding strong acid, moderate base, high temperatures and intense radiation),[45,46] as well as biological stability (neither degradation nor chemical modification compounds were identified after cells' uptake),[47,48] their solubility in both polar and nonpolar solvents,[37] and their amphiphilicity.[49–52] Besides these, the 3D cylindrical shape of the small anionic metallabis(dicarbollides) molecules with a size of 1.1 × 0.6 nm, producing strong dihydrogen B–H···H–N bond interactions with the amine groups of amino acids,[53–55] proteins,[56,57] lipids,[58] DNA[48] and glycolipids,[59] has gained significant interest in the medicinal chemistry field. For therapeutic applications, metallacarboranes can act as multimodal anticancer agents by enabling a simultaneous approach

This journal is © The Royal Society of Chemistry 2022

J. Mater. Chem. B, 2022, **10**, 9794–9815 | **9795**
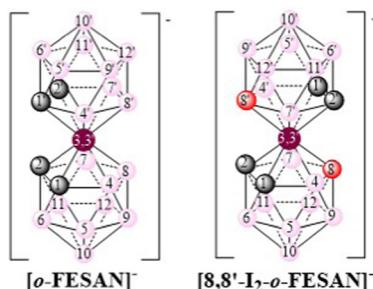
Scheme 1 Schematic representation of the small anionic ferrabis(dicarbollide) clusters with their vertices numbered. Circles in grey correspond to $C_{cluster}$−H vertices while the pink and the red ones to B−H and B−I vertices, respectively.

to chemotherapy, radiotherapy and imaging, through the incorporation of multifunctional hybrid molecules (which introduce the concept of small molecules for multitherapeutic use). Their iodinated derivatives can have additional benefits as radiosensitizers, enhancing the local dose inside tumors upon exposure to electromagnetic radiation.[60,61]

The present study aims to explore the biological potential of [o-FESAN]$^-$ and [8,8′-I$_2$-o-FESAN]$^-$ (Scheme 1) as radiosensitizers in a glioblastoma cell model, since an efficient intracellular uptake of these compounds is a crucial factor affecting radiation therapy efficacy.[61] Scheme 1 shows the formulae of the two small anionic ferrabis(dicarbollide) molecules with their vertices numbered.

As metallabis(dicarbollide) and its diiodinated derivative cross the cell membrane,[47] studies on the translocation of [o-FESAN]$^-$ and [8,8′-I$_2$-o-FESAN]$^-$ anions through synthetic lipid membranes which could reveal important properties at the interface of biological and synthetic membranes are reported, as well as their *in vivo* evaluation using the small organism *C. elegans*. The radiobiological effects induced by electromagnetic radiation (γ-rays and X-rays) in glioblastoma cells treated with Na[o-FESAN] and Na[8,8′-I$_2$-o-FESAN] are also reported. A preliminary study on the biological effects generated by a proton–boron nuclear fusion reaction (PBFR, see Scheme 2)[62] with ferrabis(dicarbollides) in the U87 glioblastoma cells is reported. We have tested for the first time this reaction using metallacarboranes to enhance proton irradiation effects through the generation of short range ($\sim$30 μm) high-LET alpha particles thus evaluating compounds' clinical relevance for this treatment modality.

2. Materials and methods

2.1. Chemistry

The sodium salts of ferrabis(dicarbollide) Na[o-FESAN] and Na[8,8′-I$_2$-o-FESAN] were synthesized from Cs[o-FESAN][42] and Cs[8,8′-I$_2$-o-FESAN][63] by using a cationic exchanging resin as reported in the literature[64] (see ESI,† Scheme S1). 1,2-Dioleoyl-*sn-glycero*-3-phosphocholine (DOPC) and 1,2-dioleoyl-*sn-glycero*-3-phosphoethanolamine (DOPE) were purchased from Avanti

Polar Lipids (Alabaster, AL). Hexadecane and pentane were purchased from Merck KGaA (Darmstadt, Germany).

2.2. Instrumentation

FTIR spectra were obtained using a Shimadzu FTIR-8300 spectrophotometer. The ^{1}H and ^{1}H{^{11}B} NMR (400.13 MHz) and ^{11}B and ^{11}B{^{1}H} NMR (128.37 MHz) spectra were recorded on a Bruker ARX 400 instrument equipped with appropriate decoupling accessories. All NMR spectra were performed in d$_6$-acetone at 22 °C. The ^{11}B and ^{11}B{^{1}H} NMR chemical shift values were referenced to external BF$_3$·OEt$_2$, while the ^{1}H and ^{1}H{^{11}B} NMR chemical shift values were referenced to SiMe$_4$. Chemical shifts are reported in units of parts per million downfield from reference. UV-Visible spectra (see ESI,† Fig. S1) were recorded on a double beam PharmaSpec UV-1700 series spectrophotometer from Shimadzu Corporation, operating from 200 nm to 800 nm in 1.0 cm quartz cells using 1 cm cuvettes with 0.08 mM of each ferrabis(dicarbollide), Na[o-FESAN] or Na[8,8′-I$_2$-o-FESAN] samples in water and *n*-octanol. Thermogravimetric analyses and differential Scanning Calorimetry (TGA/DSC) were performed on a Netzsch STA 449 thermal analyzer at a heating rate of 10 °C min^{-1} in an Ar atmosphere. EPR measurements were performed on a Bruker Elexsys 580 at 10 K. Spectral parameters were: field sweep 800 mT, central field 405 mT, modulation amplitude 0.1 mT, modulation frequency 100 KHz, time constant 1.28 ms and attenuation 30 dB.

2.3. EPR studies

EPR measurements on the Na[o-FESAN] and Na[8,8′-I$_2$-o-FESAN] salts at 80 K and 10 K were carried out in the solid state (see Fig. S2, ESI†). The EPR spectra at 10 K of the dried U87 glioblastoma cells after uptaking either Na[o-FESAN] or Na[8,8′-I$_2$-o-FESAN] were also obtained and compared with the EPR spectra of Na[o-FESAN] and Na[8,8′-I$_2$-o-FESAN] salts, respectively, which were taken as references (Fig. 1).

The spectrum of Na[o-FESAN] consists of a broad line superposed to the cavity signal. According to the value of the g factor for broad peak 1, which is 4.7, it can be assumed that this broad line originates from Fe(III).[65] This is additionally confirmed by a line of lower intensity positioned at a g value of 2.0, peak 4, on which six narrow lines are superimposed.[65] The Na[8,8′-I$_2$-o-FESAN] powder sample shows a broad signal of much stronger intensity at a g value of approximately 2.0. A shoulder at g = 4.7 is noticeable on that signal too. Both signals originate from Fe(III).[65,66]

Fig. 1(a), which shows the spectra of Na[8,8′-I$_2$-o-FESAN] in powder and U87 cells after the uptake of Na[8,8′-I$_2$-o-FESAN], diplays that, after Na[8,8′-I$_2$-o-FESAN] uptake, U87 cells contain a clear line of weak intensity at g = 1.7, while Fig. 1(b) shows a very broad signal (indicated as 6) placed at a g value of about 2 in the spectrum of dried U87 cells after the uptake of Na[o-FESAN]; this signal undoubtedly confirms the presence of iron in the sample.

2.4. Planar bilayer electrophysiology measurements

2.4.1. Planar bilayer formation and ionic current recording after the addition of sodium salts of ferrabis(dicarbollides),

9796 | *J. Mater. Chem. B*, 2022, **10**, 9794–9815

This journal is © The Royal Society of Chemistry 2022
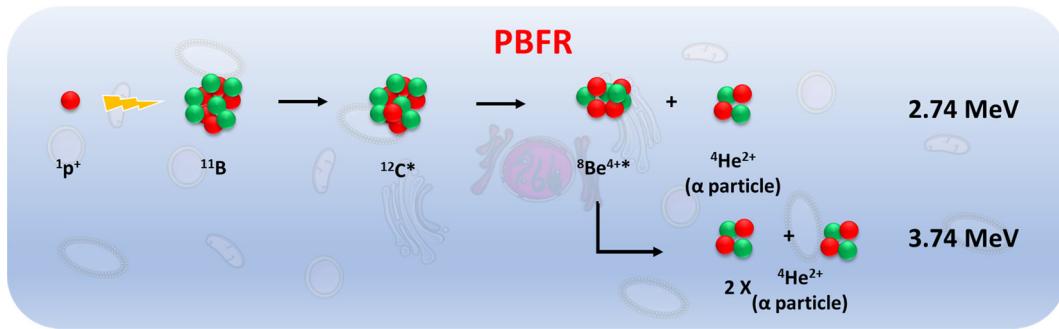
Scheme 2 Representation of the reaction between an energetic proton and ^{11}B resulting in the generation of excited carbon ^{12}C, which splits into a 2.74 MeV α particle and a ^{8}Be. Then, beryllium divides into two α particles. Consequently, a total of three α particles are generated by the proton boron reaction.
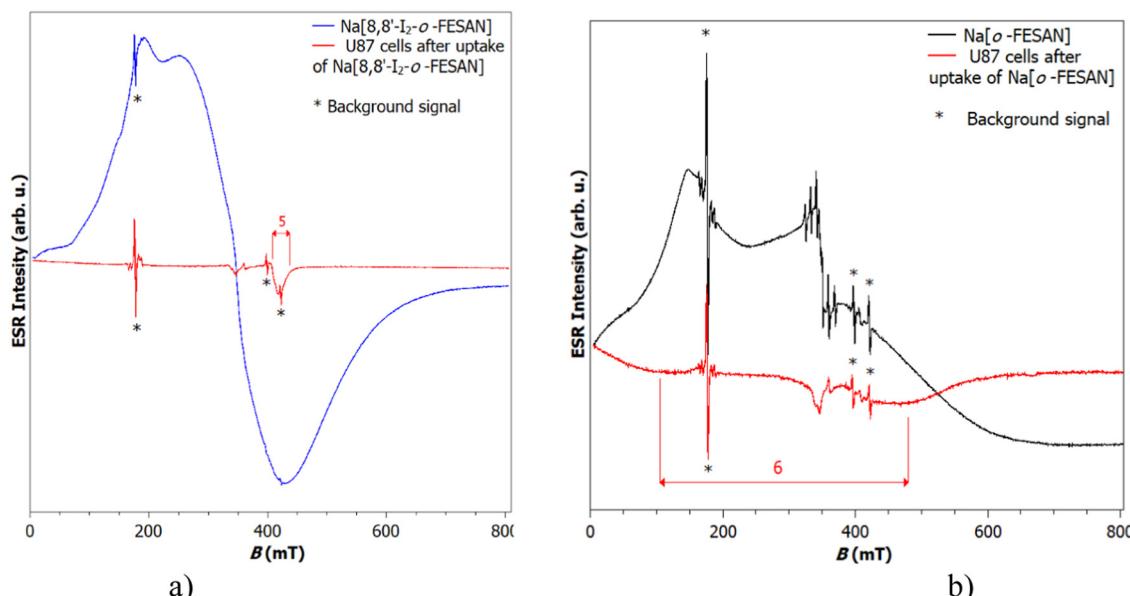
Fig. 1 (a) Spectra of Na[8,8′-I$_2$-o-FESAN] in powder, U87 cells after uptake of Na[8,8′-I$_2$-o-FESAN]. The g factor indicated by number 5 is 1.7. (b) Spectra of Na[o-FESAN] in powder and U87 cells after uptake of Na[o-FESAN]. The g factor indicated by number 6 is approximately 2.

Na[o-FESAN] and Na[8,8′-I$_2$-o-FESAN]. Lipid membranes were formed by monolayer apposition using the Montal–Mueller technique.[67,68] In brief, planar bilayers were formed by the apposition of two monolayers prepared from a 5 mg mL^{-1} solution in pentane of a mixture of DOPC and DOPE at a ratio of 7 : 3 (w/w). Lipid was added on ∼100 μm diameter orifices in the 15 μm-thick Teflon partition that separated two identical chambers (Fig. 2). The orifices were pre-treated with a 1%
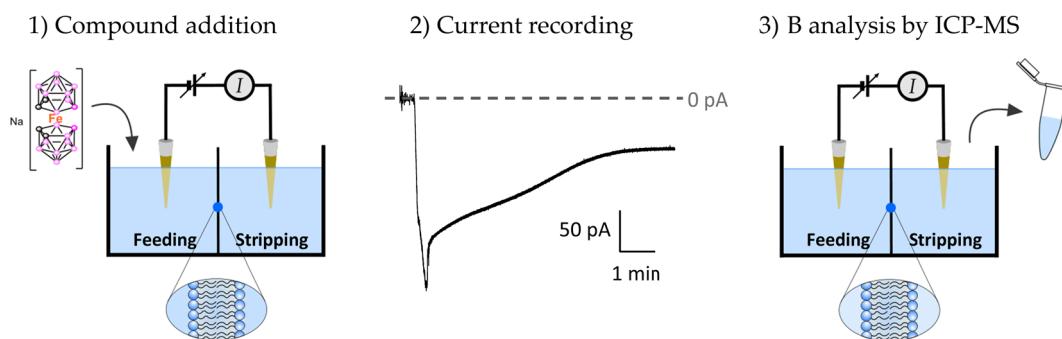
Fig. 2 Experimental method for the recording of compound-induced current in planar bilayers and determination of compound concentration in terms of the amount of boron by ICP-MS.

solution of hexadecane in pentane. Aqueous solutions consisted of 1.6 mL of 150 mM NaCl at pH 6 and all measurements were performed at room temperature (23 ± 1 °C). Planar membrane formation was tracked by applying a periodic triangular voltage wave with an external wave generator and visualizing the squared output signal with an oscilloscope. Voltage was applied through Ag/AgCl electrodes assembled in 2 M KCl, and 1.5% agarose bridges within standard 250 μL pipette tips. The potential was defined as positive when it was higher on the feeding compartment, whereas the stripping compartment was set to ground. An Axopatch 200B amplifier (Molecular Devices, Sunnyvale, CA) in the voltage-clamp mode was used to measure the current registered upon the addition of 50 μM compound at the feeding compartment of the chamber. Compound stock concentration was 10 mM in water. A constant stirring of at least 1 minute was applied after compound addition to assure homogeneous mixing. Current was filtered using an integrated low pass 8-pole Bessel filter at 1 kHz, digitized using a DigiData 1440A (Molecular Devices, Sunnyvale, CA) with a sampling frequency of 2 kHz, and analyzed using pClamp 10.7 software (Molecular Devices, Sunnyvale, CA). The chamber and the head stage were isolated from external noise sources with a double metal screen (Amuneal Manufacturing Corp., Philadelphia, PA). Current after compound addition was tracked during the entire experimental time to assure membrane integrity.

2.4.2. Determination of compound concentration. Solution from the stripping compartment was extracted 30, 60, 90 or 120 minutes after compound addition at the feeding side. Samples were sent to the Scientific Instrumentation Service of University Jaume I (Castellón, Spain) for analysis (Fig. 2). Compound concentration at the stripping side of the chamber was calculated from the boron concentration determined by inductively coupled plasma mass spectrometry (ICP-MS) using a single quadrupole mass spectrometer Thermo Scientific iCAP RQ ICP-MS (Thermo Fisher Scientific Inc., Waltham, MA). The compound translocation rate (in nM min^{-1}) of each ferrabis(dicarbollide) was calculated by dividing the obtained concentration by the experimental time of each experiment.

2.5. Cells, culture media and compound solutions

U87 glioblastoma (GBM) cells were obtained from ATCC (American Type Culture Collection). For the biological experiments, cells were cultured in DMEM with the GlutaMAX™ medium supplemented with 10% FBS and maintained at 37 °C in a 5% CO$_2$ humidified atmosphere. Fresh stock solutions (1 mM) of the ferrabis(dicarbollide) (Na[o-FESAN] and Na[8,8′-I$_2$-o-FESAN]) compounds were prepared in DMEM media. Serial dilutions from the stock were prepared in DMEM with Glutamax supplemented with 10% fetal bovine serum (FBS).

2.6. Blood–brain barrier (BBB) translocation studies

bEnd.3 murine brain endothelioma cells (ATTCC-CRL2299) were grown in DMEM supplemented with 10% FBS (all from Invitrogen) in a humidified atmosphere of 95% air and 5% CO$_2$ at 37 °C (Heraeus, Germany), with the medium being changed every other day. To allow the formation of a stable *in vitro* BBB model, 5000 cells per well were seeded in fibronectin-coated tissue culture PET inserts (pore size of 1 μm) for 24-well plates (BD falcon) and grown for 9 days with media being changed every 2 days, as previously described.[69]

For the evaluation of the integrity of the BBB model, fluorescein isothiocyanate-dextran with a MW of 4 (FD4 from Sigma Aldrich) was used as a fluorescent probe, as previously described.[68] Only cells present in the inserts with values of integrity higher than 90% were used for subsequent studies. For the translocation assay, inserts were incubated with 100 μM of Na[o-FESAN] and Na[8,8′-I$_2$-o-FESAN] in the transport medium (DMEM fluorobrite + 10% FBS) in the apical side for 5 h. After incubation, samples were collected and analyzed by ICP-MS for quantification of the B and Fe contents. Control inserts with only transport media or DMSO control were also submitted to the same procedure. After the translocation assay, inserts were washed (apical and basal sides) twice with PBS and once with the transport medium and a post-translocation integrity assay was performed as described above. For ICP-MS determination of B and Fe contents on the apical and basal fraction, each sample was incubated for 24 h with a mixture of HNO$_3$ and HCl (1:3), diluted with ultra-pure water and analyzed on a Thermo-X series spectrometer.

2.7. Viability assays with 2D cells

U87 cells were seeded in 96-well plates (1 × 10^4 cells/200 μL medium) and incubated at 37 °C for 24 h to adhere. Then, the medium was discarded, and cells were incubated with the corresponding sodium salt of the ferrabis(dicarbollide) compounds at serial concentrations in the range of 1–500 μM for 6, 24, 48 and 72 hours. After incubation, the viability was determined using the MTT assay. Two independent assays were performed, using at least 6 replicates per condition in each assay. For the MTT assay, the culture medium was removed and 200 μL of MTT solution (0.5 mg mL^{-1}) were added to each well. After incubating for 3 h at 37 °C, the MTT solution was discarded and 200 μL of DMSO were added to dissolve the formazan crystals. The absorbance was measured at 570 nm using an ELISA plate reader. Absorbance readings from treated samples were normalized to controls and curve fitting was performed using Graph Pad Prism 5 software to obtain the IC$_{50}$ values.

2.8. Cellular uptake by PIXE

The concentrations of Fe in pellets of U87 cells, controls and samples incubated with the compounds (50 μM, 24 h) were determined by the particle-induced X-ray emission (PIXE) technique using the CTN/IST Van de Graaf accelerator. The cell pellets were obtained by centrifugation after washing the cells with PBS to remove the medium and freeze-dried until use. The detailed procedure encompassing acid digestion and analysis was previously described.[70,71] The elemental concentrations of Fe were obtained in μg g^{-1} dry weight and converted to ng 10^{-6} cells.

2.9. 3D spheroid cultures

U87 spheroids were prepared in Nunclon™ Sphera™ ultra-low attachment 96U-well plates. Briefly, cells from 80–90% confluent

9798 | *J. Mater. Chem. B*, 2022, **10**, 9794–9815

This journal is © The Royal Society of Chemistry 2022

monolayer cultures were tripsinized and seeded at 1000 cells per well. The plate was then centrifuged at 1500 rpm for 5 minutes and incubated at 37 °C in a humidified atmosphere of 5% CO_2. Spheroid growth was monitored daily using a Primovert Inverted ZEISS Microscope (objective 4×) with an integrated HDcam camera, and the images were analysed using Spheroid-Sizer, a free high-throughput MATLAB-based image analysis-software program.[72] When the spheroids reached diameters in the range of 350 μm (typically at day 3), viability assays were performed.

2.10. Viability assays with 3D spheroids

U87 cells were cultured as spheroids for 3 days. Then, 100 μL of culture medium were removed from each well and 100 μL of each compound at selected concentrations were added. As a control, spheroids were incubated with 100 μL of medium supplemented with 10% FBS. After 72 hours of incubation, viability was determined using the acid phosphatase (APH) assay. Three independent assays were performed, using at least 4 spheroids per condition in each assay. In parallel, U87 cells in the monolayer incubated under the same conditions were also tested in a 96-well plate (three independent assays with at least 4 wells per condition). For the APH assay, 180 μL of culture medium was removed from each well and the spheroids were washed twice with 180 μL PBS. Then 100 μL of PBS was removed from each well and 100 μL of acid phosphatase buffer (0.1 M sodium acetate, 0.1% (v/v) Triton X-100, and 2 mg mL^{-1} p-nitrophenylphosphate pH 4.8) was added to the wells. As a negative control, 100 μL of PBS and 100 μL of acid phosphatase buffer were added to empty wells. After 90 minutes at 37 °C in a humidified atmosphere of 5% CO_2, 10 μL of 1 M NaOH was added to each well to stop the reaction, and the absorbance was measured at 405 nm using a microplate reader.

2.11. *In vivo* studies in *C. elegans*

C. elegans Bristol strain N2 and *Escherichia coli OP50* were obtained from the Caenorhabditis Genetics Center (Minnesota, USA). Nematodes were maintained using standard procedures[73] and exposure towards materials was performed following previous protocols.[74]

The survival rate of synchronized L4 nematodes was evaluated after 24 h exposure to Na[o-FESAN] and Na[8,8′-I$_2$-o-FESAN] at concentrations ranging from 0–50 μM in the M9 buffer supplemented with 4% of dead OP50 in a final volume of 100 μL. After exposure, worms' survival was computed by tapping the plate and counting the moving alive worms.[73]

Each well contained 15 ± 3 L4 worms (number of total worms (n) = 450, number of independent experiments (N) = 3). LD$_{50}$ was calculated using GraphPad Prism 9 and fitting the curve to a four-parameter dose-response curve.

2.12. Irradiation studies

For the irradiation studies, U87 cells (10^4 cells per well) were seeded into 96 well plates and previously incubated with the compounds at selected concentrations for 24 h.

2.12.1. γ-rays and X-rays. For the γ irradiation studies, cells were irradiated with a ^{60}Co γ-ray source (1530 keV) using an *AECL Eldorado 6 Irradiator*, Medical Manufacturer and Model installed in the Metrology Laboratory of Ionizing Radiation at CTN/IST. Calibrations: air Kerma and absorbed dose to water products with a cumulative dose of 2 Gy and field size of 20 × 20 cm. The uniformity of the dose rate was guaranteed for the entire cell plate (10 × 10 cm).

For the X-ray irradiation studies, cells were irradiated using a Philips MCN 165 X-ray tube and an YXLON 9421 high-voltage generator at 1.5 Gy radiation dose, 15 min@20 mA. ISO beam quality N150 was used (E_{max} = 150 keV), filtered with 4 mm Al + 1 mm Cu. The source distance to the cell plate was 0.8 m.

2.12.2 Protons. Proton irradiation was performed in the U87 cells using the external microbeam facility installed at the nuclear microprobe of the CTN/IST Van de Graaff accelerator.[75]

A 2.0 MeV proton beam was extracted from the vacuum chamber to air using an exit nozzle with a 6.3 μm thick Mylar window and focused to tens of micrometer dimensions.

The focused beam with an average flux of 2.32×10^8 protons cm^{-2} s^{-1} was scanned over a monolayer of U87 cells, which were seeded in 96-well plates (10^4 cells per well) and incubated with the compounds for 24 h. The plate was positioned perpendicular to the beam path and for each well an area of 0.11 cm^2, representing 34% of the total area of the well (0.32 cm^2) was irradiated. The culture medium was partially removed from each well immediately before irradiation to guarantee that the irradiation area would have an equivalent cell thickness of 30 μm. The proton energy was tuned to reach the main resonance energy of the proton–boron nuclear fusion reaction (675 keV) in the cell layer.[62,76] This was achieved by using an appropriate combination of attenuators (an air path of 1.34 cm and a 12.6 μm thick Mylar foil) so that the transmitted proton energy after crossing a 30 μm cell layer was 477 ± 28 keV, resulting in an average LET of 26.4 ± 0.9 keV in the cell layer. An estimated average dose of 9 Gy was delivered in each well. The stopping power and the ion range calculations were performed using the SRIM software code.[77]

2.13. Apoptosis analysis

U87 cells in the medium were seeded in 24-well plates (2 × 10^5 cells/500 μL medium) and incubated at 37 °C for 24 h to adhere. Then, the medium was discarded, and cells were incubated with Na[o-FESAN] and Na[8,8′-I$_2$-o-FESAN] at 200 and 100 μM, respectively, for 6 h. After this, cells were irradiated with the ^{60}Co γ-ray source at 2 Gy total dose. After treatment, cells were fixed with 4% (w/v) formaldehyde for 15 minutes, washed 3 times with PBS and then stained for 15 minutes with 7.5 μg mL^{-1} Hoechst 33258 in PBS (Thermo-Fisher Scientific, maximum excitation wavelength: 352 nm, maximum emission wavelength: 461 nm). After being washed 3 times with PBS, cells were observed using a Ti-U Eclipse inverted fluorescence microscope and respective software (Nikon, Tokyo, Japan) using a DAPI fluorescence filter cube (Nikon). At least 5 images with *circa* 30 nuclei were acquired using the NIS Elements Basic software (Nikon).[78]

This journal is © The Royal Society of Chemistry 2022

J. Mater. Chem. B, 2022, **10**, 9794–9815 | **9799**

2.14. Cell cycle evaluation

The cell cycle evaluation followed previously described procedures with a few modifications.[79] Briefly, U87 cells were seeded in 24-well plates (2×10^5 cells/500 μL medium) and incubated at 37 °C for 24 h to adhere. Then, the cells were synchronized in the early S phase with a thymidine double block (2 mM per well). After this, the medium was discarded and cells were incubated with the compounds at 200 μM (Na[o-FESAN]) and 100 μM (Na[8,8′-I₂-o-FESAN]) for 6 h. After this, cells were irradiated with the ^{60}Co γ-ray source at 2 Gy total dose and the medium was changed by a fresh one. After 24 h incubation, cells were detached using Tryple Express (Thermo Fisher Scientific), washed 3 times with PBS and fixed overnight in 80% (v/v) cold ethanol. After centrifugation at $1500 \times g$ for 10 minutes, cells were incubated for 30 minutes with 50 μg mL^{-1} RNAse A in PBS (NZYtech), followed by incubation with 25 μg mL^{-1} propidium iodide. Cell fluorescence was acquired using an Attune acoustic focusing cytometer (Thermo Fisher Scientific) with a BL2 filter and the results were processed with respective software (Attune Cytometric Software 2.1).

2.15. γ-H2AX assay

U87 cells were seeded in 6-well plates containing a coverslip for each well, at a density of 2×10^5 cells/500 μL medium and, after overnight attachment, were incubated with 200 μM Na[o-FESAN] or 100 μM Na[8,8′-I₂-o-FESAN] for 6 h before being irradiated as described above for the apoptotic and cell cycle assays. After 30 minutes of incubation in a fresh medium, the detection of DNA double stranded breaks was performed using the y-H2AX assay as previously described.[80] Foci analysis was made using a custom ImageJ macro, with images obtained from two independent experiments.

2.16. Colony formation assay

Analysis of colony formation was done after irradiation. U87 cells were seeded in 96-well plates and left to adhere. After 24 h, the cells were incubated with increasing concentrations of Na[o-FESAN] and Na[8,8′-I₂-o-FESAN] for 24 h and irradiated with the different sources of radiation: gamma rays (2 Gy), X-rays (1.5 Gy) and protons (9 Gy). For comparison, non irradiated cells subjected to the same protocol were used as the control. After irradiation, the cells were dissociated with

Trypsin and the number of cells was counted. Three wells per condition were used. Dissociated cells were then seeded in 6-well plates: 200 cells under control conditions, 400 cells under the conditions where cells were only exposed to radiation or incubated with the lowest concentration of both compounds, 600 cells under the conditions where cells were incubated with the intermediate concentration of the compounds, and 800 cells under the conditions where cells were incubated with the highest concentration of the compounds. After 11 days of incubation at 37 °C, cells were fixed with a solution of 3 : 1 methanol:acetic acid at −20 °C for 20 min, washed, and then stained with 4% Giemsa in phosphate buffer for 10 min. Colonies with more than 50 cells were counted. One assay was performed. Results are expressed as a ratio of cellular survival upon treatment when compared with untreated control.

2.17. Statistical analysis

The data presented in the paper are shown as mean values ± SD and, unless otherwise stated, at least 3 biological replicates were used. Statistical analysis was performed using the GraphPad Prism 6 software to assess if there was a significant effect of each treatment compared with the respective control samples. For this, a one-way ANOVA followed by Dunnett's test was performed with a threshold of $p \leq 0.05$.

3. Results

3.1. Physical and chemical properties of ferrabis(dicarbollide) molecules

As mentioned in the introduction, several reports have been published on the properties of [o-COSAN]$^-$ and [8,8′-I₂-o-COSAN]$^-$ but to the best of our knowledge, seldom related to [o-FESAN]$^-$ and [8,8′-I₂-o-FESAN]$^-$ (Table 1).[81–90]

The aqueous solubility (S) and lipophilicity (P) of a compound are key parameters in drug development.[89] Importantly, although the sodium salts of ferrabis(dicarbollides) are soluble in water (1247 and 374 mM for Na[o-FESAN] and Na[8,8′-I₂-o-FESAN], respectively), they display lipophilic character (P values are 45.7 (log P = 1.66) for Na[o-FESAN] and 99.3 (log P = 2.00) for Na[8,8′-I₂-o-FESAN]).[65]

These results indicate that the presence of the two iodine atoms significantly affects the lipophilicity of the small ferrabis(dicarbollide) molecule making the 8,8′-di-iodinated

Table 1 Summary of several physical and chemical properties of the small anionic ferrabis(dicarbollide) molecules[64]

Compound	[o-FESAN]$^-$	[8,8′-o-I₂-FESAN]$^-$
Size (Å)	1.1×0.6[63]	1.1×0.8[45]
MW	323.75	572.45
Rotamer	Cisoid	Transoid
DLS	Aggregates in H₂O (d = 140 nm) in the range $1 < c < 50$ mM; (d = 108 nm) at $c > 50$ mM	Aggregates in H₂O (d = 83 nm) in the range $1 < c < 80$ mM; (d = 1.5 nm) at $c > 80$ mM
Solubility (mM)	1247	374
log S	3.10	2.57
Lipophilia (P)	45.7	99.3
log P	1.66	2.00
$E_{1/2}$ Fe$^{3+/2+}$ (in V vs. F$_c^+$/F$_c$)	−1.00	−0.86
UV-visible (nm)	271/295	289/343

9800 | J. Mater. Chem. B, 2022, **10**, 9794–9815

This journal is © The Royal Society of Chemistry 2022

derivative approximately 2.17-fold more lipophilic than Na[o-FESAN]; whereas it is reported that Na[8,8′-I$_2$-o-COSAN] has a partition value (P = 151.0) approximately 3.5-fold higher than Na[o-COSAN] (P = 43.7).[47] Fe makes both ferrabis(dicarbollides) less lipophilic than their related cobaltabis(dicarbollides).

Lipophilicity is a major factor influencing passive brain transfer across the BBB in either direction. It is reported that typically, for a radiotracer to be considered as a potential efficient molecular imaging probe in the living human brain with positron emission tomography (PET), its partition coefficients (log P) should range between 2.0 and 3.5.[91] Consequently, the log P of Na[8,8′-I$_2$-o-FESAN] complex is in this range (see Table 1).

The TGA/DSC studies of Na[o-FESAN] and Na[8,8′-I$_2$-o-FESAN] showed that only removal of water molecules coordinated to the sodium cation was observed until 550 °C, demonstrating the thermal stability of both ferrabis(dicarbollide) clusters (see ESI,† Fig. S3 and S4). The stability of Na[o-FESAN] and Na[8,8′-I$_2$-o-FESAN] in water as well as in DMEM (without phenol red) in the absence and in the presence of FBS was studied by using FTIR and ^{11}B{^{1}H} NMR spectroscopies, which are essential analytical tools for structure elucidation and chemical determination. Recently, we have reported by using Synchrotron Radiation-Fourier Transform Infrared (FTIR) that Na[o-COSAN] after its uptake by two different glioma initiating cells (mesenchymal and proneural) strongly interacts with DNA and proteins modifying their secondary structure, while the interaction with lipids is weaker, being enough to cross the biological membranes (cell and nucleous).[58] This finding has been possible because Na[o-COSAN] displays a strong and characteristic ν(B–H) frequency in the infrared range 2.600–2.500 cm^{-1} in which no other frequencies of organic compounds appear.[92] The interaction between Na[o-COSAN] and proteins can also be observed by ^{11}B{^{1}H}NMR spectroscopy.[48] To our knowledge, neither FTIR nor ^{11}B{^{1}H}NMR studies related to the interaction between small anionic ferrabis(dicarbollide) molecules and biomolecules have been reported.

Consequently, in this article, both spectroscopies have been performed to provide information on the stability of Na[o-FESAN] and Na[8,8′-I$_2$-o-FESAN] in DMEM and DMEM + 10% FBS (Fig. 3 and 4).

Fig. 3 clearly displays that the characteristic ν(B–H) frequency of Na[o-FESAN] in DMEM (red) decreases with respect to its spectrum in an aqueous solution (blue) but the frequency decreases much more if the DMEM culture medium contains 10% FBS (dark blue); to emphasize that the characteristic B–H's frequency in the infrared range 2.600–2.500 cm^{-1} is not present in DMEM nor in the DMEM + 10% FBS, the spectra of these culture media without ferrabis(dicarbollides) were run as references. Furthermore, the N–H stretching frequency of the culture medium shifts 170 cm^{-1} to lower wavenumbers. The decrease of the ν(B–H) signal intensity and the shift of the ν(N–H) to lower frequencies are probably due to the existence of the dihydrogen B–H···H–N bonds. It seems that most of the B–H units are within the aggregates, preventing them from interacting with the IR radiation.

Furthermore, Fig. 4 clearly shows that the resonances of the ^{11}B{^{1}H} NMR spectrum corresponding to a 2 mM aqueous solution of Na[o-FESAN] (green) decrease in the ^{11}B{^{1}H} NMR spectrum in culture medium at the same concentration (red) and disappear in DMEM containing 10% FBS (light blue). Fig. 3(b) and 4(b) show the same studies for Na[8,8′-I$_2$-o-FESAN].

To discern if the ferrabis(dicarbollide) interaction with proteins affects the relaxation times, the ^{11}B{^{1}H}-NMR spectra of 2 mM Na[o-FESAN] in different solvents (aqueous solution, in 0.1 M phosphate buffer, in DMEM and in DMEM + 10% FBS) were obtained with relaxation time parameters of 2.62 s and 0.015 s (see the ESI†). No differences were observed confirming that the ferrabis(dicarbollide)–protein aggregate formation does not affect the relaxation time.

To visualize the ferrabis(dicarbollide)–protein aggregate formation, DLS measurements of a DMEM + 10% FBS solution with increasing amounts of Na[o-FESAN] were obtained. As shown in Fig. 5, the size is maintained between 0 and 0.5 mM but, at the Na[o-FESAN] concentration higher than 0.5 mM, the FBS size grows consistently.

The latter results are analogous to the studies performed with Na[o-COSAN] in DMEM that were related with the Na[o-COSAN]
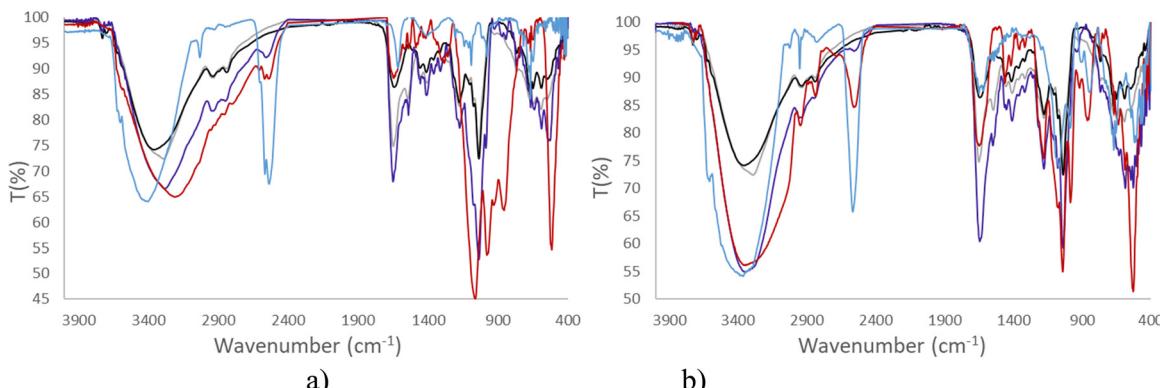

Fig. 3 (a) IR spectra of 2 mM Na[o-FESAN] in aqueous solution (blue), in DMEM (without phenol red) (red), and in DMEM + 10% FBS (purple). (b) IR spectra of 2 mM Na[8,8′-I$_2$-o-FESAN] in aqueous solution (blue), in DMEM (red), and in DMEM + 10% FBS (purple). As a control: IR spectra of DMEM (black) and DMEM + 10% FBS (grey).
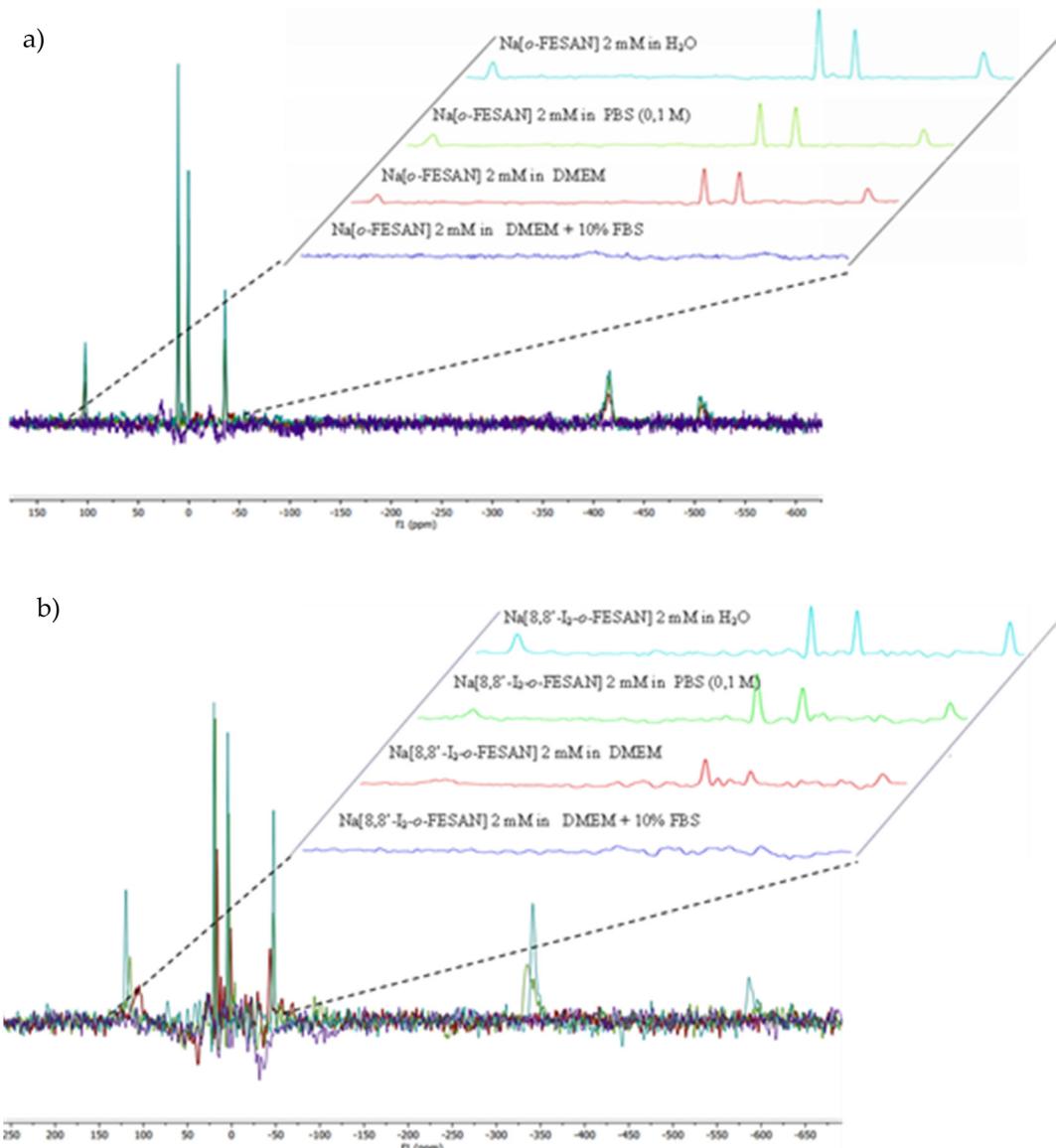
Fig. 4 (a) The $^{11}B\{^1H\}$-NMR spectrum of 2 mM Na[*o*-FESAN] in aqueous solution (blue), in 0.1 M phosphate buffer (green), in DMEM (red), and in DMEM + 10% FBS (purple). (b) $^{11}B\{^1H\}$-NMR spectrum of 2 mM Na[8,8′-I$_2$-*o*-FESAN] in aqueous solution (blue), in 0.1 M phosphate buffer (green), in DMEM (red), and in DMEM + 10% FBS (purple).
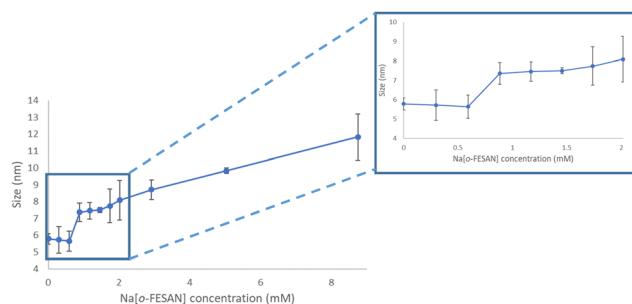
**Fig. 5** Graphical representation of the hydrodynamic diameter (nm) of the DMEM + 10% FBS culture medium measured by DLS *versus* increasing concentrations of Na[*o*-FESAN] in water in the concentration range from 0 to 9 mM.

aggregate formation in the presence of protein in DMEM and DMEM + 10% FBS.[48] The observed signals' decrease in the $^{11}B\{^1H\}$ NMR spectrum of the Na[*o*-COSAN] in DMEM without FBS is probably due to the B–H···H–N hydrogen bond between Na[*o*-COSAN] and the L-glutamine (3.4 mM) present in the medium. Interactions between [*o*-COSAN]$^-$ and several amino-acids (histidine, arginine and tryptophan),[53] as well as bioactive molecules (isoniazid, pyrazinamide, dopamine, nicotinic acid, nicotinamide, histamine and metformin) were previously observed.[54] Both spectroscopy studies support that the ferrabis-(dicarbollides) interact also with amino acids and FBS protein as they do with DNA.[48]

3.1.1 *In vitro* permeabilization of cell-free lipid membranes. To study the permeabilization of cell membranes by Na[*o*-FESAN] and Na[8,8′-I$_2$-*o*-FESAN], we investigated the interaction of these

two compounds with cell-free artificial lipid bilayer membranes of known lipid composition. We had used in our earlier experiments on Na[o-COSAN] and Na[8,8′-I$_2$-o-COSAN], neutral DOPC lipid bilayers,[93] aiming to exclude lipid charge effects on the compound translocation. Here, we used a mixture of DOPC and DOPE lipids to improve the membrane integrity and stability in the presence of both compounds and to get a lipid composition of the model membrane better resembling that of the cell membrane, which includes lipids with a negative intrinsic curvature like DOPE. After membrane formation, the compound at 50 μM final concentration was added to the feeding (*cis*) side of the chamber. Membrane permeabilization by each compound was monitored in real time by recording the ionic current across the membrane in the absence of any applied voltage (see Fig. 2). A few minutes after a transient burst, current reached a steady negative value (Fig. 6), which was reproducible in all experiments with each type of compound, although with variable values among experiments for the peak and steady currents.

Quantitative estimation of the amount of [o-FESAN]$^-$ and [8,8′-I$_2$-o-FESAN]$^-$ that crossed the membrane was made by extracting the stripping solution from the stripping side 30, 60, 90 and 120 min after compound addition to the feeding side (independent experiments) and analysing the boron content of the sample by ICP-MS (see Fig. 2). Only experiments in which the lipid membrane integrity was preserved were considered. Interestingly, the success rate of experiments with [8,8′-I$_2$-o-FESAN]$^-$ (41%) was half of that with [o-FESAN]$^-$ (85%). This result (48 *vs* 100) is consistent with the higher lipophilicity of [8,8′-I$_2$-o-FESAN]$^-$ over [o-FESAN]$^-$ (45% *vs* 100%, respectively). The concentration of the compound in the feeding side (50 μM) was chosen not too high to avoid lipid membrane disruption but high enough to match the lowest detection limit of the ICP-MS equipment (nanomolar range).

The rate of translocation of [o-FESAN]$^-$ and [8,8′-I$_2$-o-FESAN]$^-$ across the DOPC:DOPE membranes is somewhat similar: 2.6 ± 2.8 and 2.5 ± 1.8 nM min^{-1}, respectively. For both compounds, experiments show a high variability. It is known[65] that at the concentration used here both compounds form large aggregates (140 nm and 83 nm in diameter for Na[o-FESAN] and Na[8,8′-I$_2$-o-FESAN], respectively) that exceed by far the thickness of the lipid bilayers ($\sim$4–5 nm). The high variability of the translocation rate could be related to the bilayer formation technique. As is known,[67] only the central part of the membrane assembled in the orifice is actually a bilayer. The size of the central annulus where the thickness is the smallest is not known and this may change from one experiment to another. Given the fact that Na[o-FESAN] and Na[8,8′-I$_2$-o-FESAN] partition into the lipid membrane, the average effective membrane thickness might change their translocation rate, thus explaining its variability between independent experiments.

We also observed that there is no correlation between the measured ionic current in the steady state and the compound rate of translocation across the membrane (measured from ICP-MS analysis of the stripping side). Presently, there is no clear explanation of this fact but the formation of aggregates of different sizes could be a reason why both magnitudes seem to be not correlated.

3.2. Biological studies

3.2.1 *In vitro* cytotoxicity studies. The cytotoxicity of Na[o-FESAN] and Na[8,8′-I$_2$-o-FESAN] against the U87 cells was evaluated before irradiation to help the selection of the most adequate concentrations for the subsequent studies. Results given by the IC$_{50}$ values are presented in Table 2. For cells treated with Na[o-FESAN] high cellular viability was observed up to 48 h incubation. However, cells treated with the corresponding iodinated compound Na[8,8′-I$_2$-o-FESAN] presented much lower viability at the same incubation times.

3.2.2 Analysis of cellular uptake. As the therapeutic effectiveness relies on the cellular amount and distribution of compounds, we have evaluated quantitatively the net Fe uptake in U87 cells. The cellular uptake of Fe in whole U87 cells by PIXE after incubation with 50 μM of both Na[o-FESAN] and Na[8,8′-I$_2$-o-FESAN] for 24 hours is presented in Table 3. Na[8,8′-I$_2$-o-FESAN] is much more cytotoxic than its non-iodinated congener. The selected concentration of 50 μM at 24 h incubation was a compromise in order to assure that the time and concentration were adequate to allow the compound to enter the cells and deposit a high amount of Fe and concomitantly B, taking into consideration that the cells have natural iron in relatively high content. Therefore, it was important to distinguish the iron levels of untreated and treated cells. The evaluation of Fe by the PIXE technique is quite accurate but as the percentage of compound that enters the cells is usually very low it was important to measure an amount of iron far superior to the physiological levels. Anyway, the number of cells was counted at the end of the incubation time to express the
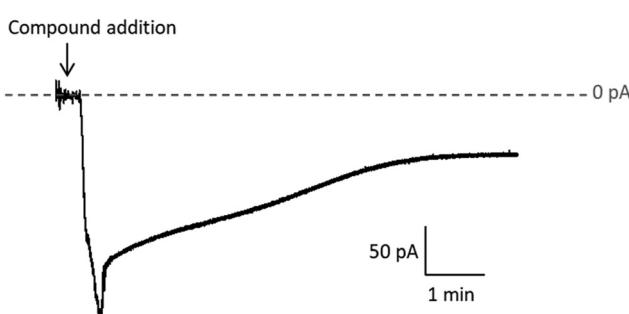

Fig. 6 Sample current recording after Na[o-FESAN] addition to the feeding side of the chamber. The stripping side was electrically grounded. Negative current implies that the [o-FESAN]$^-$ anion crosses the membrane.

Table 2 The effect of the time of exposure on the IC$_{50}$ values of ferrabis(dicarbollides) in the U87 cells. Values are shown as the mean $\pm$ SD

Incubation time (h)	U87 cells	
	Na[o-FESAN] (μM)	Na[8,8′-I$_2$-o-FESAN] (μM)
6	265 ± 118	106 ± 28
24	245 ± 92	32.1 ± 9.5
48	90.8 ± 22	7.7 ± 1.8
72	51.2 ± 12	6.0 ± 1.2

This journal is © The Royal Society of Chemistry 2022

J. Mater. Chem. B, 2022, **10**, 9794–9815 | 9803

Table 3 Cellular uptake of Fe in whole U87 cells by PIXE. Cells were previously incubated with the compounds at 50 μM for 24 h. The Fe levels in the whole cells was expressed in ng Fe/10^6 cells. Values are shown as mean ± SD

24 h, 50 μM	ng Fe/10^6 cells
Control	81.0 ± 2.8
Na[o-FESAN]	548 ± 16
Na[8,8-I$_2$-o-FESAN]	349 ± 9.4

level of Fe/10^6 cells and, at this step, only viable cells (trypan blue stain viable cells) were counted.

PIXE results showed that the Fe uptake in U87 treated cells was 4- to 6-fold higher than that in the control (non-treated cells). However, as can be observed, the cellular uptake is not related to the cytotoxic activity, since the uptake of a more active compound was less by the cells.

3.2.3 Blood–brain barrier (BBB) translocation studies. The evaluation of the ability of the both ferrabis(dicarbollides) to translocate the BBB was performed with the *in vitro* bEnd.3 cell model. The cells were grown in fibronectin-coated transwell filters, enabling the establishment of a tight monolayer of cells. Before incubation with the compounds, the integrity of the BBB model was assessed with a fluorescent probe and only inserts with >90% integrity were used. Then, bEnd3 cells were exposed at the apical side to 100 μM of Na[o-FESAN] and Na[8,8′-I$_2$-o-FESAN] for 5 h, and the B and Fe contents in the apical and the basolateral media were determined by inductively coupled plasma mass spectrometry (ICP-MS). The translocation efficiency was determined by the amount of B or Fe detected in the basolateral medium as a % of the total content (apical + basolateral media).

In Fig. 7, the % of B and Fe detected in the apical and basal fractions of cells incubated with 100 μM of Na[o-FESAN] and Na[8,8′-I$_2$-o-FESAN] is presented.

The ICP-MS determination of the content of both elements in the 2 fractions for each compound shows similar values (Na[o-FESAN]-B was compared with Na[o-FESAN]-Fe and Na[8,8′-I$_2$-o-FESAN]-B with Na[8,8′-I$_2$-o-FESAN]-Fe), which indicates that the metallacarboranes are able to cross the BBB

model intact, *i.e.*, without disruption of the 3D cluster structure. Furthermore, the ratio of the total mass detected of B *vs.* Fe is also in accordance with an intact cluster (the B/Fe ratio detected experimentally: 3.3 for Na[o-FESAN] and 2.9 for Na[8,8′-I$_2$-o-FESAN] *vs.* those predicted: 3.5 and 3.1, respectively).

The translocation results show that both ferrabis(dicarbollides) are able to translocate the *in vitro* BBB cell model, although to a different extent, with Na[8,8′-I$_2$-o-FESAN] presenting a higher translocation value (~50%) than Na[o-FESAN] (~40%), which could be correlated with its higher lipophilicity.

A post-translocation integrity assay was also performed and no decrease in the integrity of the cell model was detected, indicating the non-toxic character of both ferrabis(dicarbollides) at the time and concentration tested in the BBB model.

3.2.4 GBM spheroids' viability. The spheroids were exposed to both ferrabis(dicarbollides) on the 3rd day of culture in three different doses. The concentrations of each compound were chosen based on the IC$_{50}$ values previously determined for the monolayer culture of this cell line at 72 h, using the MTT assay (Table 2), and using a lower (0.5× IC$_{50}$) and a higher concentration (1.5–5× IC$_{50}$) for each compound.

After 72 h of exposure to the compounds (6th day of spheroid culture), the viability of the U87 spheroids was assessed by the acid phosphatase (APH) assay. A physical characterization of the spheroids upon incubation with the compounds, which included the measurement of the diameter, area, and circularity, was performed daily, from day 3 to day 6 of culture.

Illustrative microscope images of the spheroids exposed to the compounds tested at concentrations equivalent to the IC$_{50}$ and higher than the IC$_{50}$ are shown in Fig. 8.

In a qualitative analysis, the administration of the compounds did not seem to significantly affect the shape and integrity of the spheroids. Quantitatively, concerning the growth and size of the spheroids, Na[o-FESAN] affected the growth of the U87 spheroids with a significant decrease in the spheroids' area on day 3 of treatment (Fig. 8 panels A and B) for IC$_{50}$ and higher than IC$_{50}$ concentrations tested.

Overall, the circularity of the spheroids was not severely affected by the administration of the ferrabis(dicarbolide)
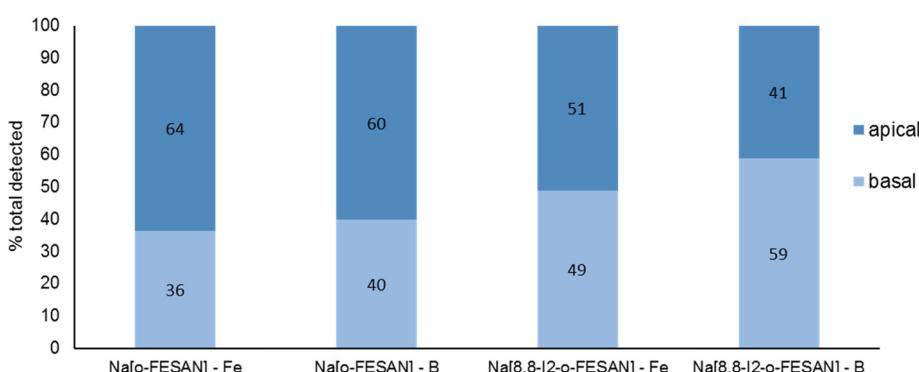
Fig. 7 BBB translocation determined by ICP-MS determination of B and Fe and in the apical and basal media of the BBB cell model incubated with 100 μM Na[o-FESAN] and Na[8,8′-I$_2$-o-FESAN] for 5 h.

9804 | *J. Mater. Chem. B*, 2022, **10**, 9794–9815

This journal is © The Royal Society of Chemistry 2022
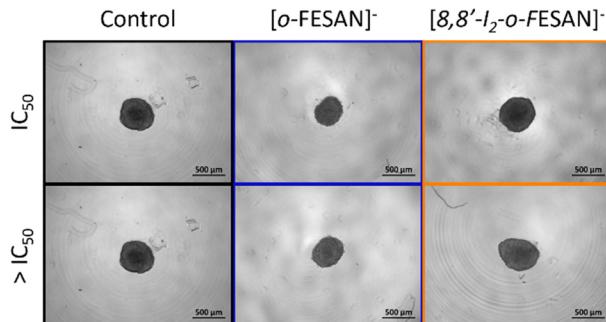
Fig. 8 Representative images of the U87 spheroids after 72 h (day 6 of culture) of exposure to the different complexes at the IC_{50} concentration and above IC_{50} concentration. Controls consist of spheroids incubated only with medium. Scale bars correspond to 500 μm.

compounds, maintaining, in most cases, a regular shape, which is reflected by circularity values very close to 1.

The viability of the spheroids after incubation with the ferrabis(dicarbollides), Na[o-FESAN] and Na[$8,8'$-I_2-o-FESAN], for 72 h was determined using the APH assay and the test was performed in parallel also for monolayer-cultured cells. The viability results of the spheroids for the 2 compounds with the IC_{50} and above IC_{50} concentrations tested are presented in Fig. 9 panels C and D. In general, these results reflect the growth behaviour observed for the spheroids.

There was an obvious decrease in the viability of the spheroids treated with all the compounds. However, using the concentration corresponding to the IC_{50} previously determined in monolayer-cultured cells by the MTT assay, only incubation with Na[o-FESAN] led to a statistically significant decrease in the spheroids' viability (Fig. 8 panel C). When using a higher
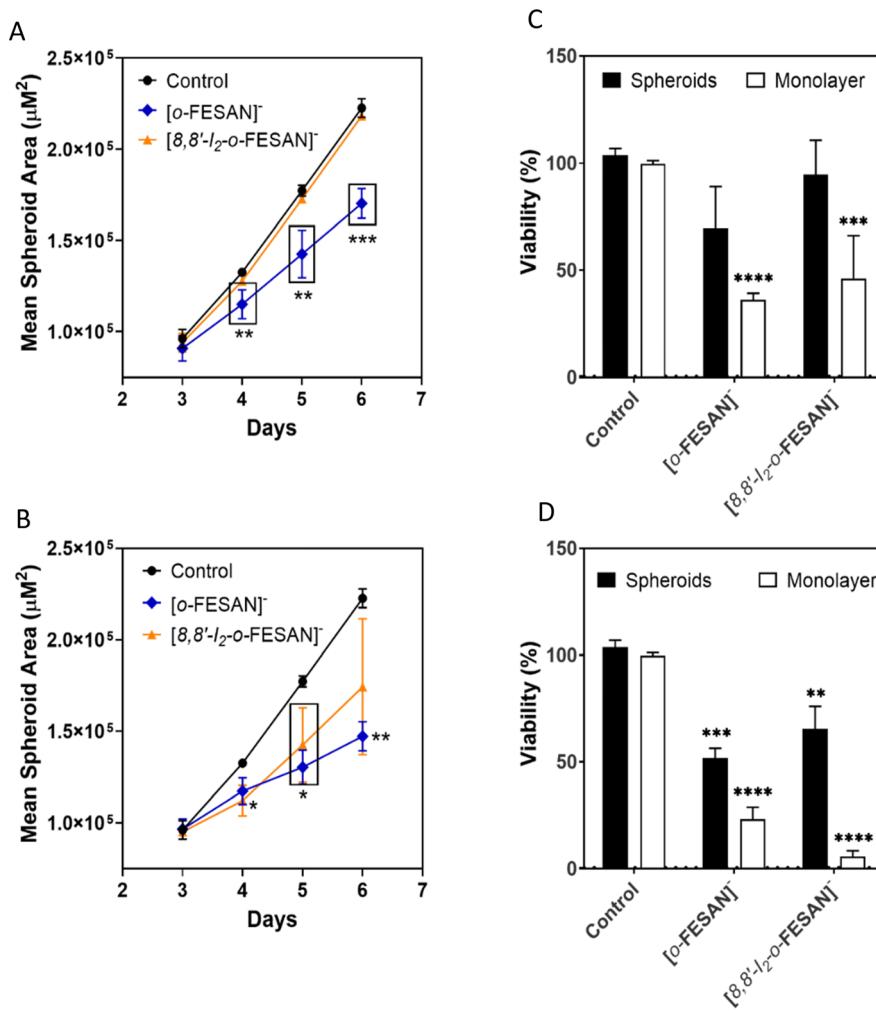
Fig. 9 Effect of exposure to Na[o-FESANE] and Na[$8,8'$-I_2-o-FESANE] on U87 spheroids at concentrations corresponding to the IC_{50} (top panels) and above the IC_{50} (bottom panels). (A) and (B) U87 spheroid growth, represented by the mean spheroids area (in μm^2) as a function of the number of days in culture, and (C) and (D) cellular viability (%) at 72 h, assessed by the APH assay, in parallel to monolayer cultured cells. Controls consist of spheroids or monolayer cultured cells incubated only with medium. Data are presented as the average ±SD of 3 independent assays for spheroids and one for monolayer cells. Statistical significance was calculated using one-way ANOVA, followed by Dunnett's test comparing treated spheroids/cells with control spheroids/cells (*$p \leq 0.05$, **$p \leq 0.01$, and ***$p \leq 0.001$).

This journal is © The Royal Society of Chemistry 2022

J. Mater. Chem. B, 2022, **10**, 9794–9815 | **9805**

concentration (Fig. 9 panel D), all compounds were found to be able to significantly reduce U87 spheroids' viability.

The same assay was performed in parallel for monolayer-cultured cells (Fig. 9 panels C and D). When compared with 3D spheroids, U87 cells grown as monolayer cultures were more sensitive to the compounds tested. This is not surprising as 3D culture systems are frequently more refractory to anti-cancer treatments due to limited drug penetration and activation of several resistance mechanisms.[94] In fact, spheroid models can mimic the metabolic and proliferative gradients of *in vivo* tumors, with consequent changes in the cellular phenotype and status, exhibiting multicellular chemoresistance.

3.2.5 *In vivo* toxicity in *Caenorhabditis elegans* (*C. elegans*). *In vitro* experiments using cultured cells were complemented with the *in vivo* evaluation of both Na[*o*-FESAN] and Na[8,8′-I$_2$-*o*-FESAN] using the invertebrate *C. elegans*, which offers the advantage of a physiological environment in which several cellular processes occur simultaneously.

To screen the toxicity of Na[*o*-FESAN] and Na[8,8′-I$_2$-*o*-FESAN] in nematodes, synchronized L4 *C. elegans* were exposed to both small molecules at concentrations ranging from 0–50 μM for 24 h (Fig. 10 panel A). Toxicity was determined by the survival of the worms (existence of movement) and the

mean lethal dose 50% (LD$_{50}$). The obtained LD$_{50}$ values for Na[*o*-FESAN] and Na[8,8′-I$_2$-*o*-FESAN] were 5.8 ± 0.6 μM and 6.0 ± 0.6 μM (Fig. 10 panel B). Na[*o*-FESAN] LD$_{50}$ was lower than the IC$_{50}$ found in U87 cells after 72 h of treatment, whereas Na[8,8′-I$_2$-*o*-FESAN] LD$_{50}$ was close to the described IC$_{50}$ for the same compound in U87 cells after 72 h. In comparison with other metallacarboranes, LD$_{50}$ values of Na[*o*-FESAN] and Na[8,8′-I$_2$-*o*-FESAN] are slightly lower than those found for Na[*o*-COSAN] and Na[8,8′-I$_2$-*o*-COSAN], 8.6 and 9.7 μM respectively.[95]

Both ferrabis(dicarbollides) arrested the worm's development in the L4 stage, the initial stage in the toxicological evaluation, whereas control worms continue their growth till adulthood (Fig. 10 panels C and D). Moreover, worms exposed to the highest concentration (50 μM) were colored by the characteristic colour of each compound, maroon for Na[*o*-FESAN] and dark green for Na[8,8′-I$_2$-*o*-FESAN], indicating the availability to cross *C. elegans* biological membranes *in vivo*.

The difference found between the IC$_{50}$ in cells and *C. elegans* could be due to the differences between the models. In *in vitro* experiments, cells are independent of each other and they are not forming organs or other higher structures. These molecules have been shown to have a cytostatic effect on cells, stopping
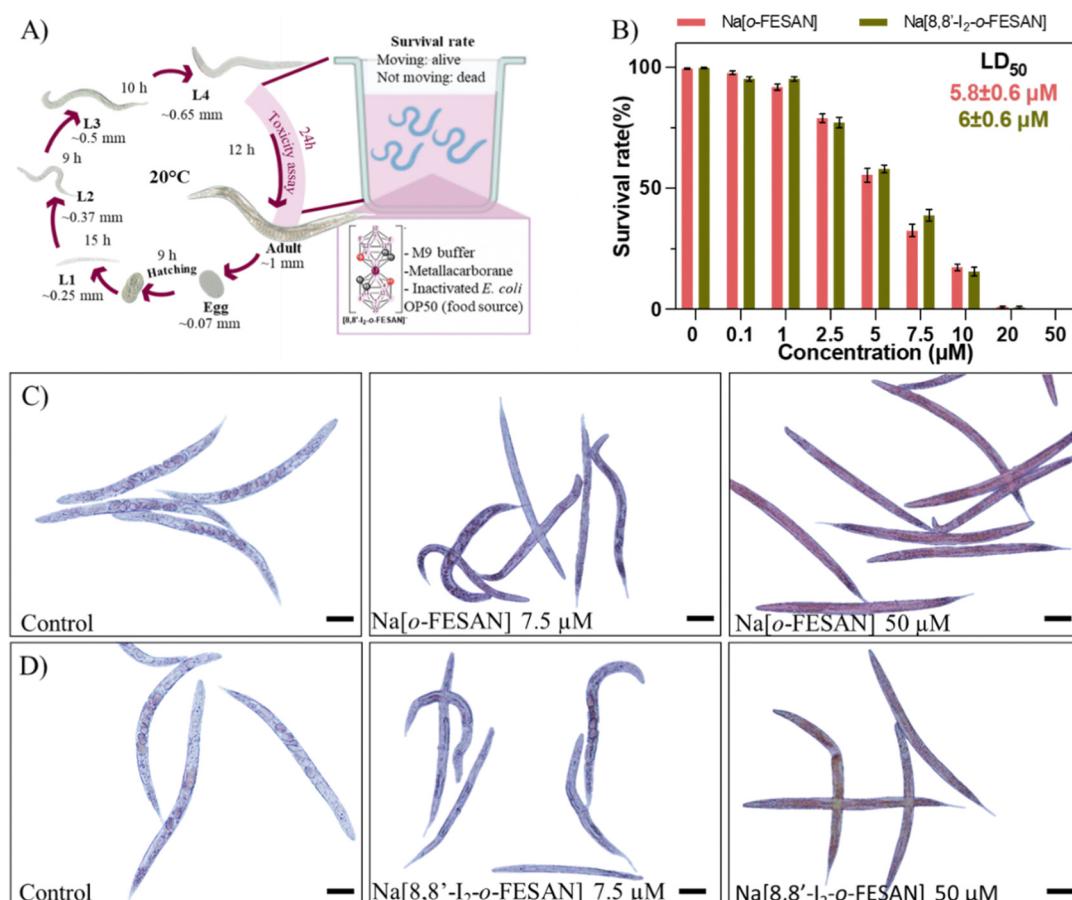

Fig. 10 *In vivo* toxicological evaluation of Na[*o*-FESAN] and Na[8,8′-I$_2$-*o*-FESAN]. (A) Schematic representation of *C. elegans* life cycle and exposure conditions from the L4 stage to adulthood. (B) Survival rate of worms at concentrations up to 50 μM Na[*o*-FESAN] (red) and Na[8,8′-I$_2$-*o*-FESAN] (green). Microscopy image of Na[*o*-FESAN]-treated worms (C) and Na[8,8′-I$_2$-*o*-FESAN]-treated worms (Na[8,8′-I$_2$-*o*-FESAN]). Bar size 100 μm.

9806 | *J. Mater. Chem. B*, 2022, **10**, 9794–9815

This journal is © The Royal Society of Chemistry 2022

their growth. After replacing the media with compounds with fresh media, cells can recover from this state. However, in animals, cells depend on each other to maintain the well-being of the whole organism, much more in simple animals such as *C. elegans*, so it is understandable to have a higher impact on them and therefore have a lower IC_{50}.

3.2.6 Biological effects upon irradiation. The U87 glioblastoma cell lines were used to assess the radiosensitizing effect by the compounds upon irradiation. For this purpose, the MTT assay and the clonogenic assay (colony formation) were used as the two most important endpoints of the radiobiological effects. These assays evaluate the effectiveness of the irradiation on the loss of cellular viability, and on the survival and proliferation of the cells, respectively.[96]

3.2.7 γ-ray irradiation. Upon γ-ray irradiation a dose dependent effect was observed for the cellular viability as shown in Fig. 11. The viability loss in comparison to control conditions (without compounds and no irradiation) was more evident at concentrations lower than the IC_{50} values for both compounds and was more pronouced for cells treated with $[8,8'\text{-}I_2\text{-}o\text{-FESAN}]^-$. In a similar way, cells presented a considerable lower survival in comparison to control conditions at concentrations lower than the IC_{50} values (Fig. 12). The cells that were incubated with $[8,8'\text{-}I_2\text{-}o\text{-FESAN}]^-$ at 100 μM had a considerable lower survival when compared to the same cells that were not irradiated but incubated with the same concentration of the compound. The MTT and the clonogenic assays showed a similar trend.

3.2.8 DNA damage by DSBs. To evaluate if the compounds under the study had a radiosensitizing ability in GBM, γ-H2AX foci detection, indicative of the occurrence of DNA DSBs, was performed by immunofluorescence microscopy.[97]

Exposure of U87 cells to any of the two compounds under study led only to a slight increase in the foci number, which was not statistically significant, indicating that the compounds by
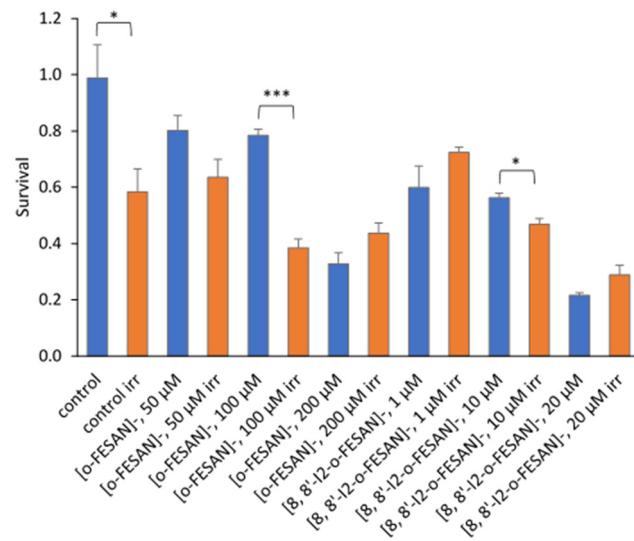

Fig. 12 Clonogenic survival fraction eleven days after irradiation with γ-rays (2 Gy) using the ^{60}Co source. U87 Cells were previously incubated with the compounds for 24 h at concentrations in the ranges of 50–200 μM ($[o\text{-FESAN}]^-$) and 1–20 μM ($[8,8'\text{-}I_2\text{-}o\text{-FESAN}]^-$). Results are mean ± SEM of a single experiment done with at least 3 replicates per condition. *p Value < 0.05; ***p value < 0.0005.

themselves do not have the ability to induce considerable DNA damage (Fig. 13 panel A). On the contrary, irradiation of control cells led to a significant increase in foci number. However, this increase was much more marked when cells had been previously exposed to 200 μM of Na$[o\text{-FESAN}]$ or 100 μM Na$[8,8'\text{-}I_2\text{-}o\text{-FESAN}]$ for 6 hours as shown in Fig. 13 panel B. More importantly, there was a significant increase in the damage induced by irradiation combined with incubation with Na$[8,8'\text{-}I_2\text{-}o\text{-FESAN}]$, when compared to the damage induced only by irradiation in control cells, which indicates
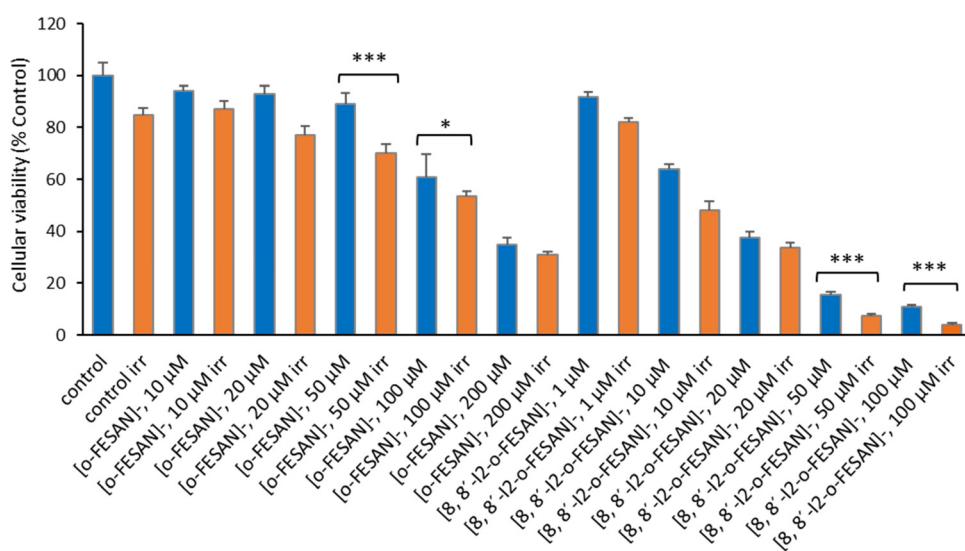

Fig. 11 Cellular viability 72 h after irradiation with γ-rays (2 Gy) using a ^{60}Co source. U87 cells were previously incubated with the compounds for 24 h at concentrations in the ranges of 10–200 μM ($[o\text{-FESAN}]^-$) and 1–100 μM ($[8,8'\text{-}I_2\text{-}o\text{-FESAN}]^-$). Results are mean ± SD of two independent experiments done with at least six replicates per condition. *$p < 0.05$; ***$p \leq 0.0005$.

This journal is © The Royal Society of Chemistry 2022

J. Mater. Chem. B, 2022, **10**, 9794–9815 | **9807**
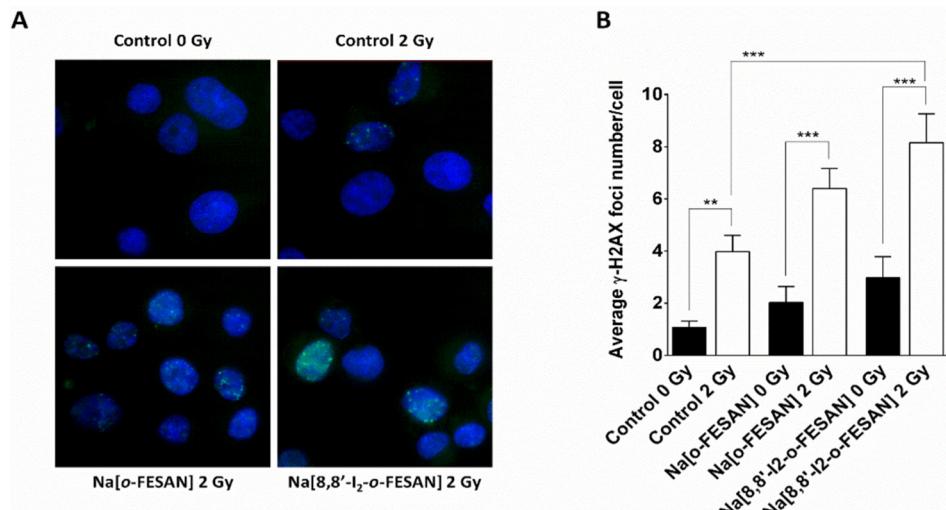
Fig. 13 γ-H2AX foci induction $\frac{1}{2}$ h post-irradiation. (A) Representative images and (B) quantification of DNA damage by 200 μM Na[o-FESAN] or 100 μM Na[8,8′-I$_2$-o-FESAN] on U87 cells upon irradiation with 2 Gy of γ-rays. The results are shown as the mean $\pm$ SEM of two independent experiments. Statistical significance was calculated using one-way ANOVA, followed by Tukey's test (**$p \leq 0.01$ and ***$p \leq 0.001$).

that Na[8,8′-I$_2$-o-FESAN] might in fact exert a potential radio-sensitizing effect in this GBM cell line.

To further understand other cellular effects of the post-irradiation of cells after exposition to Na[o-FESAN] or Na[8,8′-I$_2$-o-FESAN], apoptotic cells were visualized by fluorescence microscopy using the nucleic acid dye Hoechst 33258 (Fig. 13 panel A). As observed in Fig. 14 panel A, apoptotic events, including chromatin condensation and nucleus fragmentation were evident for [o-FESAN]$^-$ and [8,8′-I$_2$-o-FESAN]$^-$.

While in non-irradiated cells there is no statistical significant difference between control cells and cells exposed to Na[o-FESAN] or Na[8,8′-I$_2$-o-FESAN], irradiation induces an increased apoptotic events that is 3$\times$ higher in cells exposed previously to Na[o-FESAN] compared to control (Fig. 14 panel B).

Moreover, despite the slight increase in the % of apoptotic cells observed after irradiation of cells previously exposed to Na[o-FESAN], this increase is not statistically significant demonstrating the potential of Na[8,8′-I$_2$-o-FESAN] compounds as radiosensitizers.

Even if no statistically significant difference is observed between non-irradiated Na[8,8′-I$_2$-o-FESAN]-exposed compared to control cells, there is an increase of the number of apoptotic cells in non-irradiated Na[8,8′-I$_2$-o-FESAN] exposed cells compared to Na[o-FESAN] exposed cells (Fig. 14(B)).

Considering these results, cell cycle effect was evaluated by flow cytometry using propidium iodide for cell staining (Fig. 14). As observed in Fig. 15, in non-irradiated cells no effect in cell cycle progression is observed after 24 h, with a similar number of cells
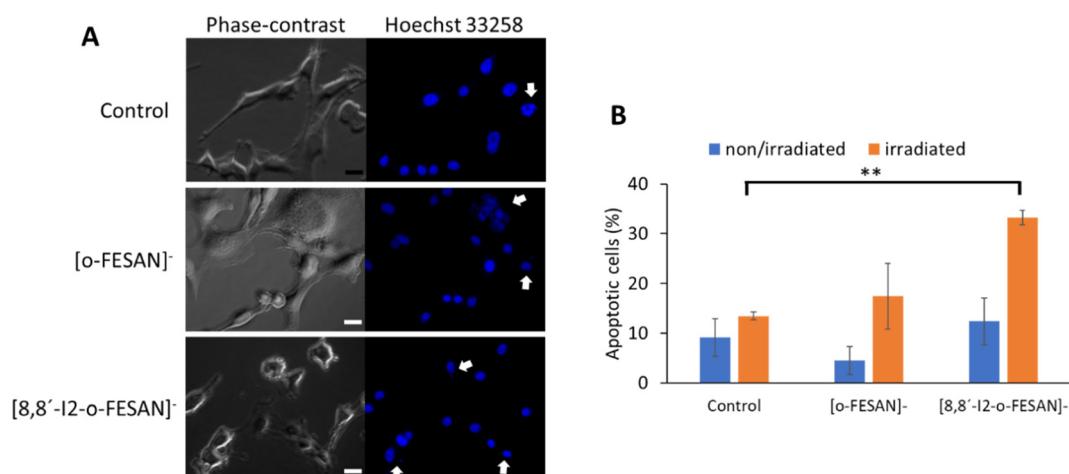
Fig. 14 Morphological changes in the nuclei of the cells exposed to 100 μM [o-FESAN]$^-$ and 100 μM [8,8′-I$_2$-o-FESAN]$^-$ with and without irradiation. (A) Nuclei of the cells stained with Hoechst 33258 for the visualization of apoptotic events, including chromatin condensation and nucleus fragmentation (white arrows) after exposure to control, [o-FESAN]$^-$ and [8,8′-I$_2$-o-FESAN]$^-$ and with irradiation. Images were obtained using a Nikon TiU eclipse and the respective software. Scale bar: 20 μm. (B) % of the apoptotic cells after exposure to [o-FESAN]$^-$ and [8,8′-I$_2$-o-FESAN]$^-$ and with and without irradiation. Six random fields with at least 10 nuclei were selected for analysis. **p Value < 0.005 relative to the respective control (control irradiated).

9808 | *J. Mater. Chem. B*, 2022, **10**, 9794–9815

This journal is © The Royal Society of Chemistry 2022
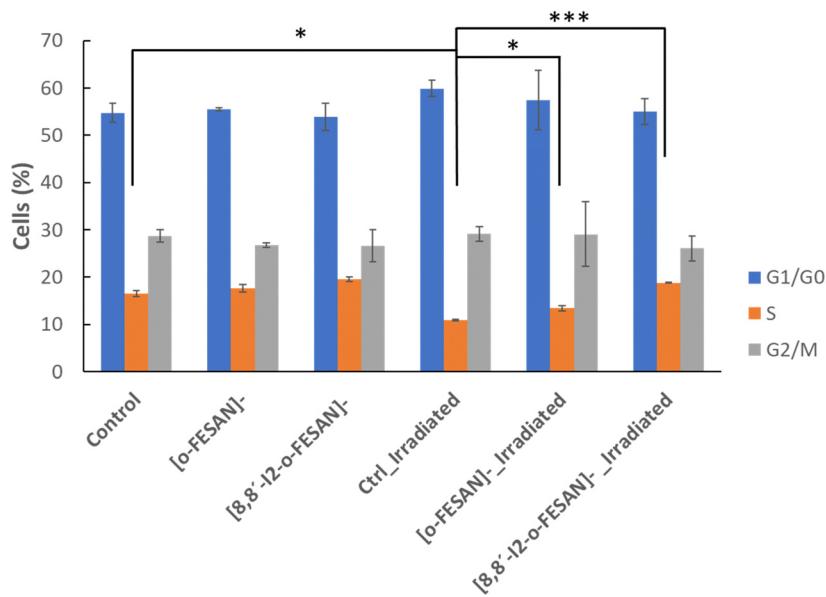
Fig. 15 Cell cycle evaluation of cells exposed to [o-FESAN]⁻ and [8,8′-I₂-o-FESAN]⁻ with or without irradiation. After two periods of synchronization at the G1/S phase with thymidine, cells were exposed to [o-FESAN]⁻ and [8,8′-I₂-o-FESAN]⁻ and irradiated. The fluorescence levels of propidium iodide were determined by flow cytometry. The represented results are the mean ± SD of two experiments. *p Value < 0.05. **p Value < 0.005.

in all phases in control, [o-FESAN]⁻ and [8,8′-I₂-o-FESAN]⁻. After irradiation, there is a slight decrease of control cells in the S phase and an increased number of cells in the G0/G1 phase. This trend is also observed in the [o-FESAN]⁻ treated cells, despite not as evident as in control cells (Fig. 15). This indicates that irradiation with γ-rays is retaining cells in the G0/G1 phase to avoid progression to the S phase.

Interestingly, when it comes to [8,8′-I₂-o-FESAN]⁻ exposed cells no difference in the number of cells in the different cell cycle phases is observed with and without irradiation (Fig. 15). However, a statistically significant difference on the number of cells in the S phase compared to control cells or cells exposed to [o-FESAN]⁻ is observed (Fig. 15).

One reason for this difference could be that the high level of γ-H2AX foci induction in cells exposed to [8,8′-I₂-o-FESAN]⁻ could induce higher levels of damage repair in cells not entering immediately into apoptosis that could, after further irradiation, survive without the need to delay the cell cycle (Fig. 13 and 15). Those cells that did not activate the repair mechanisms would be more prompt to die through apoptosis (Fig. 14 and 15).

3.2.9 X-ray irradiation. We proposed an irradiation method that utilizes fluorescence X-ray emissions from iodine. This approach should achieve a greater therapeutic effect than conventional radiotherapy. In our study [8,8′-I₂-o-FESAN]⁻ was used as the iodine-donor and [o-FESAN]⁻ was used for comparison.

The X-ray absorption edge is intrinsic for each atom. X-rays with higher energy than the K-edge of iodine (33.2 keV) are required for fluorescence X-ray emission. The irradiation was generated using two-layer metal filters containing Cu and Al. X-rays less than 31 KeV will be attenuated through Cu filter

(1 mm thick); Al filter (4 mm thick) will absorb Cu fluorescent X-ray including Kα and Kβ line (approximately 8 keV). Fluorescent X-rays including the Kα line (28.5 keV) and L-band (3.78–5.18 keV) energy bands are released from iodine. Therefore radiation damage is sustained only locally.[98]

As shown in Fig. 15 a dose dependent effect was observed for the cellular viability comparable to that obtained for γ-rays. The viability loss in comparison to control conditions (without compounds and not irradiated) was more evident at higher concentrations for both compounds. Concerning survival, cells presented a significantly lower survival in comparison to control conditions at concentrations equivalent to compounds' IC₅₀ values (Fig. 17). With the exception of cells incubated with the lowest concentration of [o-FESAN]⁻, not exposed to radiation, under all conditions cells had a significantly lower survival in comparison to control conditions (without compounds and not irradiated). The cells that were incubated with [o-FESAN]⁻ (50 and 200 μM) and [8,8′-I₂-o-FESAN]⁻ (1 and 10 μM) had a considerably lower survival when compared to the same cells not irradiated but incubated with the compounds. The MTT and the clonogenic assays showed a similar trend in particular for [8,8′-I₂-o-FESAN]⁻. However, with X-rays a considerable lower survival was observed with [8,8′-I₂-o-FESAN]⁻ treated cells in comparison to γ-rays. Although the atomic number of iron (Fe, $Z = 26$) is relatively low, a dose dependent X-ray absorption was also observed for [o-FESAN]⁻, which caused the radiosensitizing effect observed in the cells.

Results from Fig. 16 and 11 (cellular viability after irradiation with γ-rays) showed that for both [o-FESAN]⁻ and [8,8′-I₂-o-FESAN]⁻ a dose dependent effect was observed and this effect of viability loss was significant at 50 and 100 μM, although this trend was not observed at the highest concentration of

This journal is © The Royal Society of Chemistry 2022

J. Mater. Chem. B, 2022, **10**, 9794–9815 | 9809
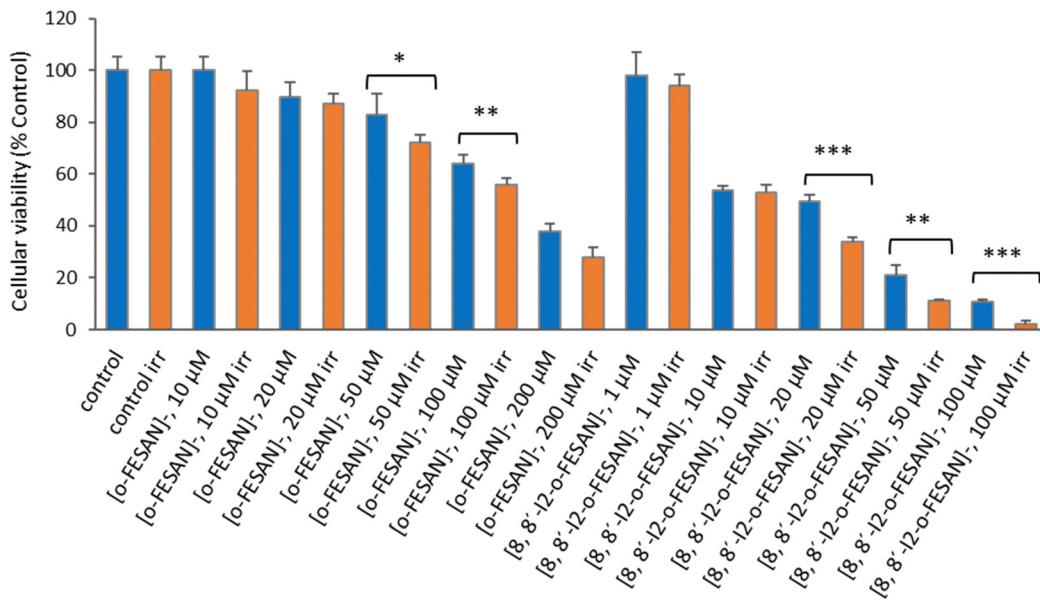
Fig. 16 Cellular viability 72 h after irradiation with X-rays (1.5 Gy) using a Philips MCN 165 X-ray tube and an YXLON 9421 high-voltage generator. U87 cells were previously incubated with the compounds for 24 h at concentrations in the ranges of 10–200 μM ([o-FESAN]$^-$) and 1–100 μM ([8,8'-I$_2$-o-FESAN]$^-$). Results are mean ± SD of two independent experiments done with at least six replicates per condition. *$p < 0.05$; **p value ≤ 0.005; and ***$p \leq 0.0005$.
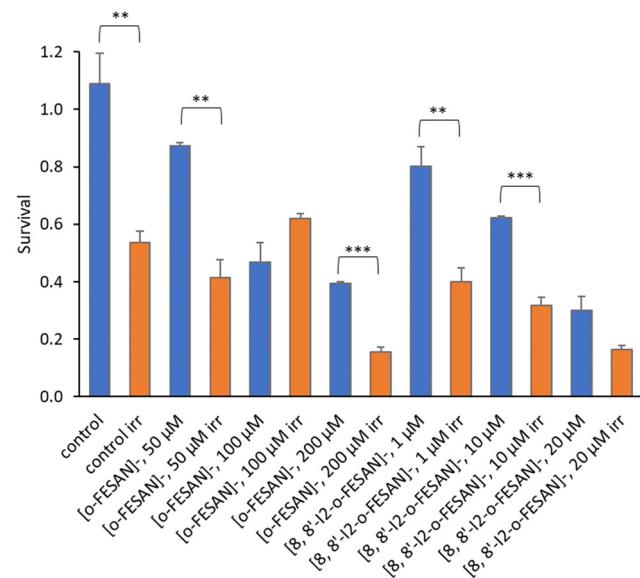
Fig. 17 Clonogenic survival fraction eleven days after irradiation with X-rays (1.5 Gy) using a Philips MCN 165 X-ray tube and an YXLON 9421 high-voltage generator. U87 Cells were previously incubated with the compounds for 24 h at concentrations in the ranges of 50–200 μM ([o-FESAN]$^-$) and 1–20 μM ([8,8'-I$_2$-o-FESAN]$^-$). Results are mean ± SEM of a single experiment done with at least 3 replicates per condition. **p Value < 0.005; ***p value < 0.0005.

[o-FESAN]$^-$ (200 μM). Both experiments were intended to check the radiosensitizing effect of iron expecting an enhanced effect of viability loss by iodine which has a high atomic number, in particular using X-rays. The fact that [8,8'-I$_2$-o-FESAN]$^-$ is much more cytotoxic could explain that the radiosensitizing effect induced by iron is somehow hindered.

3.2.10 Proton irradiation. Proton beams can offer better dose distribution due to its unique absorption profile in tissues, known as the Bragg's peak, allowing deposition of maximum destructive energy at the tumor site while reducing the dose to nearby critical tissues along their path.[99,100] This type of particle radiation has higher LET and can cause severe radiobiological effects. Therefore, proton beams may be more effective to radioresistant cancers such as brain tumours.[101]

The presence of B in the target molecule may increase the effect of protons on cell death, due to the p + ^{11}B → 3α nuclear fusion reaction, with a resonance at 675 keV and a high cross section ($\sim$1 barn).[76] The emitted α-particles have a broad spectrum with a predominant energy of 4 MeV, whose range in water ($\approx$25 μm) is of the order of a cell dimension. Due to these characteristics, the reaction has great potential in the context of therapeutic applications.

Fig. 18 shows the impact in the viability of U87 glioblastoma cells treated with [o-FESAN]$^-$ and [8,8'-I$_2$-o-FESAN]$^-$ of proton irradiation, as a function of the deposited dose.

In non-irradiated U87 cells, the treatment with [o-FESAN]$^-$ and [8,8'-I$_2$-o-FESAN]$^-$ caused a small decrease in viability relative to controls as measured by the MTT assay. However, after proton irradiation U87 cells exposed to [o-FESAN]$^-$ and [8,8'-I$_2$-o-FESAN]$^-$ showed a 50% increase in lethality contrasting with a 16% increase in irradiated controls as shown in Fig. 18. It should be considered that only 34% of the cells were directly irradiated. Therefore, the high lethality rate observed suggests that α-particles generated in the fusion reaction may have direct consequences in irradiated cells and in those contiguous to the irradiated area, such as, more complex lesions at the DNA level, and indirect effects by radiolysis. Such an expressive lethality may be the enhancement effect due to

9810 | *J. Mater. Chem. B*, 2022, **10**, 9794–9815

This journal is © The Royal Society of Chemistry 2022

Fig. 18 Cellular viability of U87 cells relative to control (non-irradiated cells) after proton irradiation. (A) Selection of irradiation time after treatment of cells with compounds at their IC_{50} values for 24 h. (B) After treatment with $[o\text{-FESAN}]^-$ (50 and 100 µM) and $[8,8'\text{-}I_2\text{-}o\text{-FESAN}]^-$ (1 and 10 µM) and proton irradiation for 10 s with a dose of 9 Gy. Results are mean ± SD of two independent experiments done with at least 3 replicates per condition. ***p Value ≤ 0.0005.

α-particles but these effects should be further evaluated. The magnitude of lethality achieved evidenced the potential of both compounds to increase the cellular killing following proton irradiation.

All cells incubated with $[8,8'\text{-}I_2\text{-}o\text{-FESAN}]^-$ (irradiated and not irradiated) had a significantly reduced survival in comparison to control conditions (Fig. 19). Cells incubated with the highest concentration of $[o\text{-FESAN}]^-$ (100 µM) also had a significant decrease in survival in relation to control conditions.

The first experimental proof of PBCT using a boronated compound (BSH) and DU145 as a prostate cancer cell model was reported by Cirrone et al.[99] The BSH concentration was selected based on the literature results on the use of BSH for BNCT. Authors found that the yield of chromosome aberrations is similar for cells irradiated with X-rays and proton only, but in the presence of BSH the number of aberrations per cell increase (0.08 vs. 0.18), when irradiated at 4 Gy. From our studies, we cannot directly compare these results with those herein presented. The main differences are: (i) a different cell model; (ii) the use of metallacarboranes having two boron clusters instead of one as in BSH; (iii) lower concentrations used compared to that used for BSH; (iv) different experimental set-up and different irradiation conditions; (v) different cell
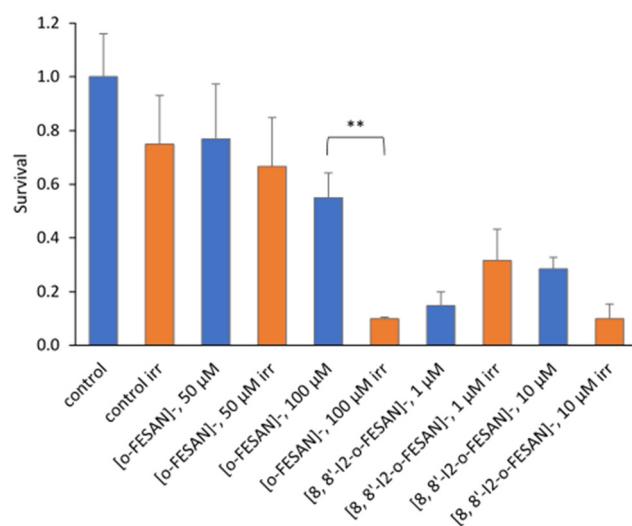
Fig. 19 Clonogenic survival fraction eleven days after proton irradiation for 10 s at a dose of 0.98 kGy. U87 Cells were previously incubated with the compounds for 24 h at concentrations in the ranges of 50–200 µM ($[o\text{-FESAN}]^-$) and 1–20 µM ($[8,8'\text{-}I_2\text{-}o\text{-FESAN}]^-$). Results are mean ± SEM of a single experiment done with at least 3 replicates per condition. **p Value < 0.005.

This journal is © The Royal Society of Chemistry 2022

J. Mater. Chem. B, 2022, 10, 9794–9815 | 9811

volume and mass as a cell monolayer was irradiated in our study; and (vi) a theoretical calculation of the dose was done; therefore, ~9 Gy in 30 μm water equivalent showed to cause a significant loss of cellular viability and survival. Nevertheless, the results herein presented constitute the first experimental evidence of a significant enhancement of proton effectiveness by the damage caused to U87 cells, in the presence of boron-rich metallacarboranes, through irradiation with proton beams. This effect was well above the cytotoxic effect of metallacarboranes against U87 cells. Although preliminar at the moment, our results represent an important finding for further development by both *in vitro* and *in vivo* studies, particularly in the treatment of glioblastoma.

4. Conclusions

Radiotherapy (RT) is a current standard-of-care treatment for glioblastoma multiform (GBM). Since GBM is a radioresistant cancer, most patients experience tumour recurrence and disease progression. Therefore, it is mandatory to find new alternatives to overcome radiation resistance. The development of multifunctional materials with additive therapeutic effects and better safety is an urgent need and a challenge in cancer therapy research. Increasing the effectiveness of radiotherapy using high-Z materials has recently attracted much attention. The present study proposes ferrabis(dicarbollide) small anions, [o-FESAN]$^-$ and [8,8′-I$_2$-o-FESAN]$^-$, as prospective radiosensitizers in GBM. As is well known the radiosensitizing effect depends on the cellular uptake, and the favorable uptake of these molecules encouraged us to study their potential for multimodal radiotherapies (Mössbauer effect, γ-rays, X-rays, BNCT and PBFT) as an "all in one" approach. Moreover, the chemical and the biological stabilities of these ferrabis(dicarbollides) in physiological media are also key parameters to be considered for prospective clinical applications. FTIR and ^{11}B{^{1}H}-NMR spectroscopies of both ferrabis(dicarbollides) in cellular media (with and without FBS) confirmed the binding affinity of ferrabis(dicarbollides) to amino acids and proteins. The study on the translocation of the small [o-FESAN]$^-$ and [8,8′-I$_2$-o-FESAN]$^-$ anions through a DOPC:DOPE synthetic lipid membrane, which include lipids with negative intrinsic curvature to better resembling the cells membrane, indicated that the translocation rate of both anions at 50 μM is similar. These studies support that the translocation process of ferrabis(dicarbollides) is not simply related to their lipophilic character.

The viability of the ferrabis(dicarbollides) was evaluated in U87 cells, monolayer and spheroids, after treatment with both ferrabis(dicarbollides). Using U87 monolayer cells, the iodinated compound was revealed to be much more cytotoxic even at shorter incubation times. When compared with monolayer cells, U87 cells grown as spheroids were less sensitive to the compounds tested, as expected due to limited drug penetration and activation of several resistance mechanisms. However, after 72 hours U87 spheroids incubated with Na[o-FESAN] at

the IC$_{50}$ concentration led to a statistically significant decrease in the spheroids' viability.

In vivo tests with both ferrabis(dicarbollide) small anions were performed in L4 *C. elegans* nematodes showing LD$_{50}$ values similar for both Na[o-FESAN] and Na[8,8′-I$_2$-o-FESAN] after 24 h of incubation. These anionic small molecules, whose interaction with amino acids and proteins has been demonstrated herein, could interact with the amine groups in the plethora of biomolecules of the *C. elegans* organism and probably contribute to their toxicity.

The development of multifunctional materials with additive therapeutic effects and better safety is an urgent need and a challenge in cancer therapy research. The radiobiological effects of radiosensitization using the ferrabis(dicarbollides) [o-FESAN]$^-$ and [8,8′-I$_2$-o-FESAN]$^-$ were studied using electromagnetic radiation, γ-ray and X-ray. The γ-ray irradiation promoted apoptosis in [o-FESAN]$^-$ and [8,8′-I$_2$-o-FESAN]$^-$ treated cells, with the latter inducing a 3-fold increase in irradiated *vs.* non-irradiated cells. Regarding the cytostatic potential of the treatment, the cell cycle analysis revealed that γ-rays retain cells in the G0/G1 phase, which is mainly observed in controls and [o-FESAN]$^-$ treated cells and to a smaller extent in [8,8′-I$_2$-o-FESAN]$^-$ treated cells. Together with DNA damage analysis, these results suggest that γ-ray irradiation in [8,8′-I$_2$-o-FESAN]$^-$ induces more DNA damage, without the possibility for cells to recover, triggering apoptosis. Exploring the ability of iodine-mediated X-ray radiation enhancement to induce DNA damage, we anticipate that [8,8′-I$_2$-o-FESAN]$^-$ has potential to be further explored in this domain. Although the atomic number of iron (Fe, Z = 26) is relatively low, both iodine and iron can also be proposed in combined radiation therapies, as radiosensitizers. We also tested for the first time the proton boron fusion reaction (PBFR) with U87 cells exposed to [o-FESAN]$^-$ and [8,8′-I$_2$-o-FESAN]$^-$, taking advantage of their high boron (^{11}B) content. The results obtained for the cellular damage suggest that proton boron fusion radiation therapy, when combined with boron-rich compounds, is a promising modality to fight against resistant tumors. Although encouraging, more developments are needed to further explore ferrabis(dicarbollides) as radiosensitizers towards a positive impact on the therapeutic strategies of GBM.

To sum up, our results of the *in vitro*, *in vivo*, and irradiation studies strongly suggest that these small anions are prospective candidates to be considered as future radiosensitizers in GBM through multimodal radiotherapies. More research is being conducted in our laboratories to enlighten on the irradiation mechanism when the cell pre-targeting with boron-containing compounds happens successfully. We hope that the continued developments in this area of metal-based radiosensitizers in cancer radiotherapy will have a positive impact on the therapeutic strategies for glioblastoma treatment. Furthermore, the strength of PBFR is that ^{11}B is the key nucleus in this radiation whereas in BNCT it is ^{10}B. In BNCT an isotopic enrichment in ^{10}B of the boron-containing drug is required whereas in PBFR it appears be not to necessary. Also, in BNCT each B results in one α-particle while in PBFR each nucleus of ^{11}B results in three

9812 | *J. Mater. Chem. B*, 2022, **10**, 9794–9815

This journal is © The Royal Society of Chemistry 2022

α-particles. A simplistic calculation indicates that the use of PBFR would require 1/12th of isotopically natural molecules with respect to BNCT. Furthermore, in an ideal situation, BNCT can be used synchronously on the existing ^{10}B and Mössbauer on ^{57}Fe, resulting in several therapies in one compound.

Author contributions

Conflicts of interest

The authors declare no conflict of interest.

Acknowledgements

References

1 D. Hanahan and R. A. Weinberg, *Cell*, 2011, **144**, 646–674.

2 H. Sung, J. Ferlay, R. L. Siegel, M. Laversanne, I. Soerjomataram, A. Jemal and F. Bray, *Ca-Cancer J. Clin.*, 2021, **71**, 209–249.

3 E. Hosseinzadeh, N. Banaee and H. A. Nedaie, *Curr. Cancer Ther. Rev.*, 2017, **13**, 17–27.

4 E. Bidram, Y. Esmaeili, H. Ranji-Burachaloo, N. Al-Zaubai, A. Zarrabi, A. Stewart and D. E. Dunstan, *J. Drug Delivery Sci. Technol.*, 2019, **54**, 101350.

5 R. Gyanchandani, N. Priedigkeit, A. Basudan and A. V. Lee, *Intratumor heterogeneity: Biological and clinical implications*, Elsevier Inc., 2018; ISBN 9780128117859.

6 R. Oun, Y. E. Moussa and N. J. Wheate, *Dalton Trans.*, 2018, **47**, 6645–6653.

7 G. Housman, S. Byler, S. Heerboth, K. Lapinska, M. Longacre, N. Snyder and S. Sarkar, *Cancers*, 2014, **6**, 1769–1792.

8 R. Baskar, K. A. Lee, R. Yeo and K. W. Yeoh, *Int. J. Med. Sci.*, 2012, **9**, 193–199.

9 N. Hunter and C. R. Muirhead, *J. Radiol. Prot.*, 2009, **29**, 5–21.

10 G. L. Jiang, *Front. Med. China*, 2012, **6**, 165–172.

11 R. F. Barth, Z. Zhang and T. Liu, *Cancer Commun.*, 2018, **38**, 36.

12 W. Sauerwein, A. Wittig, R. Mos and Y. Nakagawa, *Neutron Capture Therapy. Principles and Applications*, Springer-Verlag, Berlin Heidelberg, Germany, 2012, DOI: **10.1007/978-3-642-31334-9**.

13 A. E. Schwint, A. Monti Hughes, M. A. Garabalino, E. C. C. Pozzi, E. M. Heber and V. A. Trivillin, Optimizing the therapeutic efficacy of boron neutron capture therapy (BNCT) for different pathologies: Research in animal models employing different boron compounds and administration strategies (Chapter 3.6), in *Boron-Based Compounds. Potential and Emerging applications in Medicine*, ed. E. Hey-Hawkins and C. Viñas, John Wiley & Sons Ltd, Chichester, UK, 2018.

14 S. Imamichi and M. Masutani, *Cancer Sci.*, 2018, **109**, 753.

15 (a) J. Xu, J. Gao and Q. Wei, *J. Nanomater.*, 2016, ID8507924, DOI: **10.1155/2016/8507924**; (b) A.-G. Niculesco and A. M. Grumezescu, *Appl. Sci.*, 2021, **11**, 3626.

16 T. D. Malouff, D. S. Seneviratne, D. K. Ebner, W. C. Stross, M. R. Waddle, D. M. Trifiletti and S. Krishnan, *Front. Oncol.*, 2021, **11**, 1–11.

17 F. Tabbakh and N. S. Hosmane, *Sci. Rep.*, 2020, **10**, 1–12.

18 D. Kwatra, A. Venugopal and S. Anant, *Transl. Cancer Res.*, 2013, **2**, 330–342.

19 L. Gong, Y. Zhang, C. Liu, M. Zhang and S. Han, *Int. J. Nanomed.*, 2021, **16**, 1083–1102.

20 S. Lacombe, E. Porcel and E. Scifoni, *Cancer Nanotechnol.*, 2017, **8**, 9.

21 J. Choi, G. Kim, G. Cho, S. Bin and H. J. Im, *J. Nanobiotechnol.*, 2020, **18**, 1–23.

22 N. Goswami, Z. Luo, X. Yuan, D. T. Leong and J. Xie, *Mater. Horiz.*, 2017, **4**, 817–831.

23 M. Norouzi, *Pharmacol. Res.*, 2020, **156**, 104753.

24 S. Penninckx, A. C. Heuskin, C. Michiels and S. Lucas, *Cancers*, 2020, **12**, 1–361.

25 F. Silva, A. Paulo, A. Pallier, S. Même, É. Tóth, L. Gano, F. Marques, C. F. G. C. Geraldes, M. M. C. A. Castro, A. M. Cardoso, A. S. Jurado, P. López-Larrubia, S. Lacerda and M. P. Cabral Campello, *Materials*, 2020, **13**, 1–17.

26 H. Marsudaira, A. Ueno and I. Furuono, *Radiol. Sci.*, 1980, **84**, 144–148.

27 L. S. Freudenberg, W. Jentzen, A. Stahl, A. Bockisch and A. S. J. Rosenbaum-Krumme, *Eur. J. Nucl. Med. Mol. Imaging*, 2011, **38**, 48–56.

This journal is © The Royal Society of Chemistry 2022

J. Mater. Chem. B, 2022, **10**, 9794–9815 | 9813

28 M. W. Barentsz, M. A. A. J. van den Bosch, W. B. Veldhuis, P. J. van Diest, R. M. Pijnappel, A. J. Witkamp and H. M. Verkooijen, *Br. J. Surg.*, 2013, **100**(5), 582–588.

29 N. W. P. Rutjes, B. A. Binnington, C. R. Smith, M. D. Maloney and C. A. Lingwood, *Kidney Int.*, 2002, **62**(3), 832–845.

30 L. Andreana, G. Isgro, L. Marelli, N. Davies, D. Yu, S. Navalkissoor and A. K. Burroughs, *Cancer Treat. Rev.*, 2012, **38**(6), 641–649.

31 G. Bleeker, G. A. M. Tytgat, J. A. Adam, H. N. Carona, L. C. M. Kremer, L. Hooft and E. C. van Dalen, *Cochrane Database Syst. Rev.*, 2015, **9**, CD009263.

32 M. Henze, A. Mohammed, H. P. Schlemmer, K. K. Herfarth, S. Hoffner, S. Haufe, W. Mier, M. Eisenhut, J. Debus and U. Haberkorn, *J. Nucl. Med.*, 2004, **45**(4), 579–586.

33 K. B. Gona, A. Zaulet, V. Gómez, F. Teixidor, J. Llop and C. Viñas, *Chem. Commun.*, 2014, **50**, 11415–11417.

34 A. B. H. Laster, W. C. Thomlinson and R. G. Fairchild, *Radiat. Res.*, 1993, **133**, 219–224.

35 M. Tamura, H. Ito and H. Matsui, *Sci. Rep.*, 2017, **7**, 1–7.

36 Y. Xie, Y. Han, X. Zhang, H. Ma, L. Li, R. Yu and H. Liu, *Front. Oncol.*, 2021, **11**, 1–14.

37 J. Poater, C. Vinas, I. Bennour, S. E. Gordils, M. Sola and F. Teixidor, *J. Am. Chem. Soc.*, 2020, **142**(20), 9396–9407.

38 J. Plesek, *Chem. Rev.*, 1992, **92**, 269–278.

39 R. N. Grimes, *Carboranes*, Elsevier Inc., New York, 3rd edn, 2016.

40 M. F. Hawthorne, D. C. Young and P. A. Wegner, *J. Am. Chem. Soc.*, 1965, **87**, 1818–1819.

41 M. F. Hawthorne and T. D. Andrews, *J. Chem. Soc., Chem. Commun.*, 1965, 443–444.

42 M. F. Hawthorne, D. C. Young, T. D. Andrews, D. V. Howe, R. L. Pilling, A. D. Pitts, M. Reintjes, L. F. Warren Jr and P. A. Wegner, *J. Am. Chem. Soc.*, 1968, **90**, 879–896.

43 C. Viñas, J. Pedrajas, J. Bertran, F. Teixidor, R. Kivekäs and R. Sillanpää, *Inorg. Chem.*, 1997, **36**, 2482–2486.

44 I. Bennour, A. Cioran, F. Teixidor and C. Viñas, *Green Chem.*, 2019, **21**, 1925–1928.

45 J. Rais and P. Selucky, *Nucleonics*, 1992, **1**, 17.

46 S. D. Reilly, C. F. V. Mason and P. H. Smith, *Cobalt(III) Dicarbollide: A Potential 137Cs and 90Sr Waste Extraction Agent, Report LA-11695*, Los Alamos National Laboratory, Los Alamos, NM, 1990, DOI: 10.2172/7079517.

47 M. Tarrés, E. Canetta, E. Paul, J. Forbes, K. Azzouni, C. Viñas, F. Teixidor and A. J. Harwood, *Sci. Rep.*, 2015, **5**, 7804.

48 I. Fuentes, T. García-Mendiola, S. Sato, M. Pita, H. Nakamura, E. Lorenzo, F. Teixidor, F. Marques and C. Viñas, *Chem. – Eur. J.*, 2018, **24**, 17239–17254.

49 A. M. A. Abdelgawwad, J. A. M. Xavier, D. Roca-Sanjuán, C. Viñas, F. Teixidor and A. Francés-Monerris, *Angew. Chem., Int. Ed.*, 2021, **60**, 25753–25757.

50 P. Matejícek, P. Cígler, K. Procházka and V. Král, *Langmuir*, 2006, **22**, 575–581.

51 P. Bauduin, S. Prevost, P. Farràs, F. Teixidor, O. Diat and T. Zemb, *Angew. Chem., Int. Ed.*, 2011, **50**, 5298–5300.

52 D. C. Malaspina, C. Viñas, F. Teixidor and J. Faraudo, *Angew. Chem., Int. Ed.*, 2020, **59**, 3088–3092.

53 A.-I. Stoica, C. Viñas and F. Teixidor, *Chem. Commun.*, 2009, 4988–4990.

54 A.-I. Stoica, C. Viñas and F. Teixidor, *Chem. Commun.*, 2008, 6492–6494.

55 A.-I. Stoica, C. Kleber, C. Viñas and F. Teixidor, *Electrochim. Acta*, 2013, **113**, 94–98.

56 I. Fuentes, J. Pujols, C. Viñas, S. Ventura and F. Teixidor, *Chem. – Eur. J.*, 2019, **25**, 12820–12829.

57 T. M. Goszczynski, K. Fink, K. Kowalski, Z. J. Lesnikowski and J. Boratynski, *Sci. Rep.*, 2017, **7**, 9800.

58 M. Nuez-Martínez, L. Pedrosa, I. Martinez-Rovira, I. Yousef, D. Diao, F. Teixidor, E. Stanzani, F. Martínez-Soler, A. Tortosa, À. Sierra, J. J. Gonzalez and C. Viñas, *Int. J. Mol. Sci.*, 2021, **22**, DOI: 10.3390/ijms22189937.

59 T. Merhi, A. Jonchère, L. Girard, O. Diat, M. Nuez, C. Viñas and P. Bauduin, *Chem. – Eur. J.*, 2020, **26**, 13935–13947.

60 P. Farràs, E. J. Juárez-Pérez, M. Lepšík, R. Luque, R. Núñez and F. Teixidor, *Chem. Soc. Rev.*, 2012, **41**, 3445–3463.

61 T. Peters, C. Grunewald, M. Blaickner, M. Ziegner, C. Schütz, D. Iffland, G. Hampel, T. Nawroth and P. Langguth, *Radiat. Oncol.*, 2015, **10**, 1–13.

62 D. K. Yoon, N. Naganawa, M. Kimura, M. G. Choi, M. S. Kim, Y. J. Kim, M. W. M. Law, S. K. Djeng, H. B. Shin, B. Y. Choe and T. S. Suh, *Appl. Phys. Lett.*, 2019, **115**, 223701.

63 I. Rojo, F. Teixidor, C. Viñas, R. Kivekäs and R. Sillanpää, Clusters, *Chem. – Eur. J.*, 2003, **9**, 4311–4323.

64 I. Bennour, M. N. Ramos, M. Nuez-Martínez, J. A. M. Xavier, A. B. Buades, R. Sillanpää, F. Teixidor, D. Choquesillo-Lazarte, I. Romero, M. Martinez-Medina and C. Viñas, *Dalton Trans.*, 2022, **51**, 7188–7209.

65 M. Filek, M. Łabanowska, M. Kurdziel and A. Sieprawska, *Toxins*, 2017, **9**, 178.

66 H. Zhang, C. J. Carrell, D. Huang, V. Sled, T. Ohnishi, J. L. Smith and W. A. Cramer, *J. Biol. Chem.*, 1996, **271**(49), 31360–31366.

67 M. Montal and P. Mueller, *Proc. Natl. Acad. Sci. U. S. A.*, 1972, **69**, 3561–3566.

68 S. M. Bezrukov and I. Vodyanoy, *Biophys. J.*, 1993, **64**, 16–25.

69 B. Woods, R. D. M. Silva, C. Schmidt, D. Wragg, M. Cavaco, V. Neves, V. F. C. Ferreira, L. Gano, T. S. Morais, F. Mendes, J. D. G. Correia and A. Casini, *Bioconjugate Chem.*, 2021, **32**, 1399–1408.

70 A. B. Buades, L. C. J. Pereira, B. J. C. Vieira, A. C. Cerdeira, J. C. Waerenborgh, T. Pinheiro, A. P. A. Matos, C. G. Pinto, J. F. Guerreiro, F. Mendes, S. Valic, F. Teixidor, C. Viñas and F. Marques, *Inorg. Chem. Front.*, 2022, **9**, 1490–1503.

71 M. A. Barreiros, T. Pinheiro, M. F. Araújo, M. M. Costa, M. Palha and R. C. da Silva, *Spectrochim. Acta, Part B*, 2001, **56**, 2095–2106.

72 W. Chen, C. Wong, E. Vosburgh, A. J. Levine, D. J. Foran and E. Y. Xu, *J. Visualized Exp.*, 2014, **89**, 51639.

73 S. Brenner, *Genetics*, 1974, **77**, 71–94.

9814 | *J. Mater. Chem. B*, 2022, **10**, 9794–9815

This journal is © The Royal Society of Chemistry 2022

74 L. Gonzalez-Moragas, P. Berto, C. Vilches, R. Quidant, A. Kolovou, R. Santarella-Mellwig, Y. Schwab, S. Stürzenbaum, A. Roig and A. Laromaine, *Acta Biomater.*, 2017, **53**, 598–609.

75 E. Alves, K. Lorenz, N. Catarino, M. Peres, M. Dias, R. Mateus, L. C. Alves, V. Corregidor, N. P. Barradas, M. Fonseca, J. Cruz and A. Jesus, *Eur. Phys. J. Plus*, 2021, **136**, 684.

76 M. C. Spraker, M. W. Ahmed, M. A. Blackston, N. Brown, R. H. France, S. S. Henshaw, B. A. Perdue, R. M. Prior, P.-N. Seo, S. Stave and H. R. Weller, *J. Fusion Energy*, 2012, **31**, 357–367.

77 http://www.srim.org/ (accessed 11/3/2022).

78 L. R. Raposo, A. Silva, D. Silva, C. Roma-Rodrigues, M. Espadinha, P. V. Baptista, M. M. M. Santos and A. R. Fernandes, *Bioorg. Med. Chem.*, 2021, **30**, 115880.

79 T. S. Morais, Y. Jousseaume, M. F. M. Piedade, C. Roma-Rodrigues, A. R. Fernandes, F. Marques, M. J. Villa De Brito and M. Helena Garcia, *Dalton Trans.*, 2018, **47**, 7819–7829.

80 E. Pereira, L. do Quental, E. Palma, M. C. Oliveira, F. Mendes, P. Raposinho, I. Correia, J. Lavrado, S. Di Maria, A. Belchior, P. Vaz, I. Santos and A. Paulo, *Sci. Rep.*, 2017, **7**, 42544.

81 J. D. McKinney, F. S. McQuillan, H. Chen, T. A. Hamor, C. J. Jones, M. Slaski, G. H. Cross and C. J. Harding, *J. Organomet. Chem.*, 1997, **547**, 253–262.

82 O. N. Kazheva, G. G. Alexandrov, A. V. Kravchenko, V. A. Starodub, I. A. Lobanova, I. B. Sivaev, V. I. Bregadze, L. V. Titov, L. I. Buravov and O. A. Dyachenko, *J. Organomet. Chem.*, 2009, **694**, 2336–2342.

83 O. N. Kazheva, G. G. Alexandrov, A. V. Kravchenko, I. B. Sivaev, I. D. Kosenko, I. A. Lobanova, M. Kajňaková, L. I. Buravov, V. I. Bregadze, A. Feher, V. A. Starodub and O. A. Dyachenko, *Inorg. Chem. Commun.*, 2012, **15**, 106–108.

84 J. M. Forward, D. M. P. Mingos and A. V. Powell, *J. Organomet. Chem.*, 1994, **465**, 251–258.

85 J. M. Forward, D. M. P. Mingos, T. E. Müller, D. J. Williams and Y.-K. Yan, *J. Organomet. Chem.*, 1994, **467**, 207–216.

86 R. J. Wiersema and M. F. Hawthorne, *J. Am. Chem. Soc.*, 1974, **96**, 761–770.

87 K. Bednarska-Szczepaniak, K. Dziedzic-Kocurek, E. Przelazly, J. Stanek and Z. J. Lesnikowski, *Chem. Commun.*, 2021, **58**(3), 391–394.

88 T. Garcia-Mendiola, V. Bayon-Pizarro, A. Zaulet, I. Fuentes, F. Pariente, F. Teixidor, C. Viñas and E. Lorenzo, *Chem. Sci.*, 2016, **7**, 5786–5797.

89 I. Grabowska, A. Stachyra, A. Gora-Sochacka, A. Sirko, A. B. Olejniczak, Z. J. Lesnikowski, J. Radecki and H. Radecka, *Biosens. Bioelectron.*, 2014, **51**, 170–176.

90 The compound's solubility (S) is the concentration (mol L^{-1}) of its saturated aqueous solution, while their lipophilicity is given by its n-octanol/water Partition Coefficient (P), which is defined as the ratio of the amount of compound present in the organic phase (n-octanol) to the amount present in the aqueous phase. For convenience, the $\log S$ and $\log P$ are used.

91 V. W. Pike, *Trends Pharmacol. Sci.*, 2009, **30**, 431–440.

92 L. A. Leites, *Chem. Rev.*, 1992, **92**, 279–323.

93 C. Verdiá-Báguena, A. Alcaraz, V. M. Aguilella, A. M. Cioran, S. Tachikawa, H. Nakamura, F. Teixidor and C. Viñas, *Chem. Commun.*, 2014, **50**, 6700–6703.

94 F. Mittler, P. Obeïd, A. V. Rulina, V. Haguet, X. Gidrol and M. Y. Balakirev, *Front. Oncol.*, 2017, **7**, 293.

95 M. Nuez-Martinez, C. I. G. Pinto, J. F. Guerreiro, F. Mendes, F. Marques, A. Muñoz-Juan, J. A. M. Xavier, A. Laromaine, V. Bitonto, N. Protti, S. Geninatti Crich, F. Teixidor and C. Viñas, *Cancers*, 2021, **13**, 6367.

96 K. Buch, T. Peters, T. Nawroth, M. Sänger, H. Schmidberger and P. Langguth, *Radiat. Oncol.*, 2012, **7**, 1.

97 L. J. Kuo and L.-X. Yang, *In Vivo*, 2008, **22**, 305–309.

98 M. Tamura, H. Ito and H. Matsui, *Sci. Rep.*, 2017, **7**, 43667.

99 G. A. P. Cirrone, L. Manti, D. Margarone, G. Petringa, L. Giuffrida, A. Minopoli, A. Picciotto, G. Russo, F. Cammarata, P. Pisciotta, F. M. Perozziello, F. Romano, V. Marchese, G. Milluzzo, V. Scuderi, G. Cuttone and G. Korn, *Sci. Rep.*, 2018, **8**, 1141.

100 P. Bláha, C. Feoli, S. Agosteo, M. Calvaruso, F. P. Cammarata, R. Catalano, M. Ciocca, G. A. P. Cirrone, V. Conte, G. Cuttone, A. Facoetti, G. I. Forte, L. Giuffrida, G. Magro, D. Margarone, L. Minafra, G. Petringa, G. Pucci, V. Ricciardi, E. Rosa, G. Russo and L. Manti, *Front. Oncol.*, 2021, **11**, 682647.

101 T. Mitin and A. L. Zietman, *J. Clin. Oncol.*, 2014, **32**, 2855–2863.

This journal is © The Royal Society of Chemistry 2022

J. Mater. Chem. B, 2022, **10**, 9794–9815 | 9815